# Facial shape and allometry quantitative trait locus intervals in the Diversity Outbred mouse are enriched for known skeletal and facial development genes

**Authors**

David C. Katz[1*], J. David Aponte[1], Wei Liu[1], Rebecca M. Green[1], Jessica M. Mayeux[2], K. Michael Pollard[2], Daniel Pomp[3], Steven C. Munger[4], Steven A. Murray[4], Charles C. Roseman[5], Christopher J. Percival[6], James Cheverud[7], Ralph S. Marcucio[8], Benedikt Hallgrímsson[1*]

**Affiliations**

[1] Department of Cell Biology & Anatomy, Alberta Children's Hospital Research Institute and McCaig Bone and Joint Institute, Cumming School of Medicine, University of Calgary, AB, Canada

[2] Department of Molecular Medicine, The Scripps Research Institute, La Jolla, CA, USA

[3] Department of Genetics, University of North Carolina Medical School, Chapel Hill, NC, USA

[4] The Jackson Laboratory, Bar Harbor, ME, USA

[5] Department of Animal Biology, University of Illinois Urbana Champaign, Urbana, IL, USA

[6] Department of Anthropology, Stony Brook University, Stony Brook, NY, USA

[7] Department of Biology, Loyola University Chicago, Chicago, IL, USA

[8] Department of Orthopaedic Surgery, School of Medicine, University of California San Francisco, San Francisco, CA, USA

*** Corresponding authors**

bhallgri@ucalgary.ca, david.katz@ucalgary.ca

## Abstract

The biology of how faces are built and come to differ from one another is complex. Discovering the genes that contribute to differences in facial morphology is one key to untangling this complexity, with important implications for medicine and evolutionary biology. This study maps quantitative trait loci (QTL) for skeletal facial shape using Diversity Outbred (DO) mice. The DO is a randomly outcrossed population with high heterozygosity that captures the allelic diversity of eight inbred mouse lines from three subspecies. The study uses a sample of 1147 DO animals (the largest sample yet employed for a shape QTL study in mouse), each characterized by 22 three-dimensional landmarks, 56,885 autosomal and X-chromosome markers, and sex and age classifiers. We identified 37 facial shape QTL across 20 shape principal components (PCs) using a mixed effects regression that accounts for kinship among observations. The QTL include some previously identified intervals as well as new regions that expand the list of potential targets for future experimental study. Three QTL characterized shape associations with size (allometry). Median support interval size was 3.5 Mb. Narrowing additional analysis to QTL for the five largest magnitude shape PCs, we found significant overrepresentation of genes with known roles in growth, skeletal development, and sensory organ development. For most intervals, one or more of these genes lies within 0.25 Mb of the QTL's peak. QTL effect sizes were small, with none explaining more than 0.5% of facial shape variation. Thus, our results are consistent with a model of facial diversity that is influenced by key genes in skeletal and facial development and, simultaneously, is highly polygenic.

## Author Summary

The mammalian face is a complex structure serving many functions. We studied the genetic basis for facial skeletal diversity in a large sample of mice from an experimental population designed for the study of complex traits. We quantified the contribution of genetic variation to variation in three-dimensional facial shape across more than 55,000 genetic markers spread throughout the mouse genome. We found 37 genetic regions which are very likely to contribute to differences in facial shape. We then conducted a more detailed analysis of the genetic regions associated with the most variable aspects of facial shape. For these regions, a disproportionately large number of genes are known to be important to growth and to skeletal and facial development. The magnitude of these genetic contributions to differences in facial shape are consistently small. Our results therefore support the notion that facial skeletal diversity is influenced by many genes of small effect, but that some of these small effects may be related to genes that are fundamental to skeletal and facial development.

## Introduction

The facial skeleton is a complex morphology that serves a diverse set of critical roles. It houses and protects the forebrain and most sensory organs and provides essential anatomy for oral communication, feeding, and facial expression. Structured differences (covariance) in facial shape and form depend upon variation in the biological processes that coordinate facial development [1-7]. Understanding how these processes act and combine to build a facial skeleton requires interrogation at multiple levels of the genotype-phenotype (GP) map [8, 9].

Among the most fundamental of these inquiries is the search for genetic variants that contribute to facial variation. These genetic variants are the basic building blocks of diversity

66 and, within species, circumscribe the potential for short-term evolutionary change [10, 11].
67 Over the past decade, dozens of studies in humans, mouse models, and other species have
68 dissected GP associations for the craniofacial complex using moderate-to-high density genetic
69 maps (tens of thousands to millions of markers). The focus is typically on additive effects [12],
70 though some recent work considers interactions among loci [4, 13, 14].

71 In humans, genome-wide association studies (GWAS) targeting variation in soft tissue
72 facial form have been completed for European [15-20], African [21], South American [22], and
73 Asian [23] cohorts. Collectively, the studies report around 50 loci for facial morphology [24].
74 While there is limited overlap in the candidate gene sets among studies [25], and though many
75 of the individual genes have no previously known role in facial development [3], the genes that
76 do replicate across GWAS (*PAX 1*, *PAX3, HOXD* cluster genes, *DCHS2*, *SOX9*) are known to be
77 important to facial and/or skeletal morphogenesis.

78 Compared to human studies, mapping the genetics of facial variation in mice offers
79 several benefits, including greater control over genetic and environmental variation and the
80 ability to record observations, directly or *in silico*, on the skeleton itself [14, 26-31]. In recent
81 years, the focus of mouse skull QTL analyses has expanded to include tests of enrichment for
82 disease phenotypes and roles in skull development, as well as the search for and validation of
83 candidate genes [32-34]. Dozens of QTL have been identified. As with human facial shape
84 GWAS candidates, this is encouraging but also a small beginning—on the order of the total
85 number of loci identified for human height just a decade ago [35]. Quantitative genetics
86 analyses [32, 36, 37] and expression and epigenomic atlases of facial development both
87 strongly point to the potential for hundreds or thousands of genetic loci with as-yet-undetected

88 QTL variance contributions [38-40]. Increased sample sizes, greater mapping resolution, and the
89 development of new experimental lines all have the potential to expand the facial shape QTL
90 library and increase the precision of variant localization [41-43].

91 The present study maps mouse facial shape QTL in what is, to date, the largest sample
92 yet used for this purpose (*n* = 1147). We use Diversity Outbred mice (DO; Jackson Laboratory,
93 Bar Harbor, ME), a random outcross model derived from the Collaborative Cross (CC) founding
94 lines [43-46]. The DO is specifically designed for genetic mapping of complex traits. Each
95 animal's genome is a unique mosaic of the genetic diversity present in the CC founders—more
96 than 45 million segregating SNPs [47]. Random outcrossing (of non-sibs) over many DO
97 generations maintains this diversity and increases recombination frequency, which is critical for
98 reducing confidence intervals of localized QTL [41]. Compared to classic backcross and
99 intercross designs, the combinatorial possibilities for allelic variation within and among DO
100 animals are vast. The genetic diversity in a DO sample may thus mimic diversity in the natural
101 populations that animal models are meant to illuminate.

102 We quantify facial shape with 22 three-dimensional landmarks **(Fig 1)** and estimate its
103 association with founder haplotype variation at 56,885 genetic markers. The dependent
104 observations in the QTL scans are scores on shape PCs. For each PC explaining more than 1% of
105 shape variation, we identify statistically significant marker effects using a mixed effects
106 regression model that simultaneously accounts for kinship among animals [48, 49]. We then
107 undertake a more detailed analysis of QTL intervals for shape PCs 1-5. We estimate founder
108 coefficients, test whether the overall gene set is enriched for biological processes relevant to
109 facial development and perform association mapping to highlight a list of potential causal

genes. In order to visualize and quantify the magnitude of marker effects on multivariate facial shape (as opposed to univariate PC scores), for each QTL peak, we fit an additional mixed model that accommodates high-dimensional dependent observations [50].

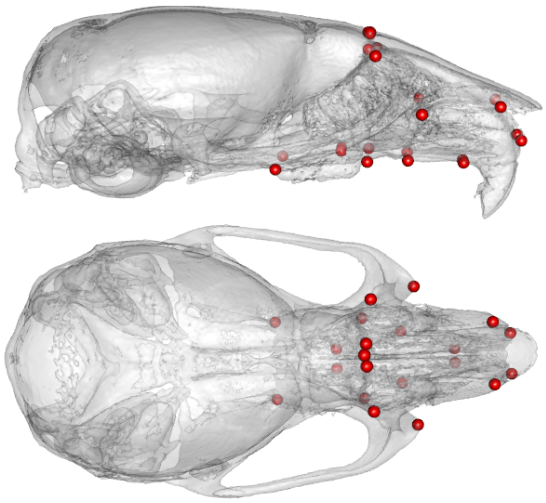

**Fig 1. Landmark map.**

## Results and Discussion

### QTL and Shape Variable Heritability

We used a mixed effects regression model to quantify GP associations between 56,885 genetic markers and each of the 20 shape PCs explaining >1% of the symmetric component of facial shape variation **(S1 Fig)**. Evidence for a QTL was evaluated by comparing logs odds (LOD) scores (likelihood ratios comparing the magnitude of marker model residuals to the residuals of a null model that excludes the marker effect) [51] at each marker to a distribution of maximum LOD scores obtained from quantifying marker effects over 1000 random permutations of GP assignments.

While comparisons to prior studies are complicated by design features unique to each, the design employed here appears to have conferred benefits in terms of QTL identification and localization, the primary objectives of QTL analysis [41]. From the 20 genome scans, 37 QTL

surpassed our threshold for statistical significance (95% quantile of the maximum LOD score distribution). Median support interval width was 3.5 Mb (mean 7.1 Mb) using a 1.5 LOD-drop threshold to define support interval boundaries. Comparable prior studies identified 17-30 QTL for the skull, with a lowest median QTL interval of 7.8 Mb (using a less-demanding 1.0 LOD-drop threshold) [32, 33].

**Fig 2** plots the support intervals for these QTL (**see also S1 Table**). The QTL span 15 of 19 autosomes as well as the X-chromosome. On chromosomes 7, 14, 15, and 17, QTL from multiple PCs have overlapping associations with the same genomic region.

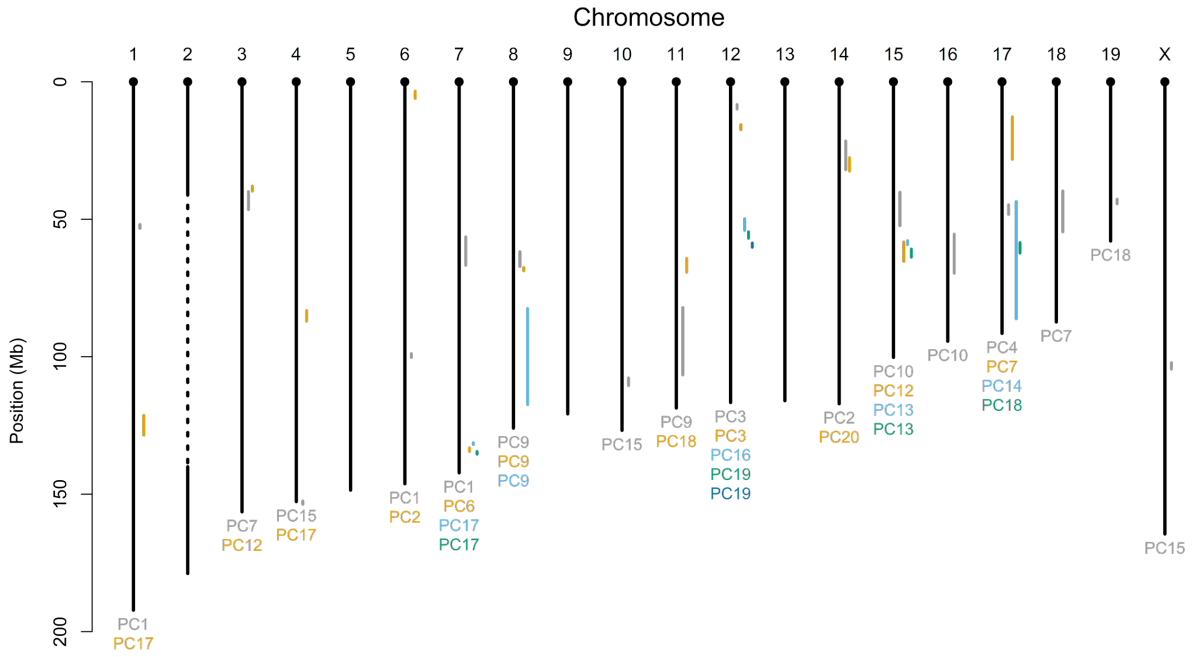


**Fig 2.** Mouse genome physical map with QTL support intervals. Intervals on the same chromosome are color coded to match the color of the PC for which the QTL was identified (listed below chromosome). The dashed line in the middle of chromosome 2 represents a region for which genetic effects were not evaluated due to the potential effects of transmission distortion on QTL identification (see Materials & Methods for further explanation).

144 For each PC, the random effect heritability estimate quantifies the proportion of
145 phenotypic variance attributable to overall genetic similarity at the founder level [49]. We
146 excluded from the genetic similarity (relatedness) calculation all markers on the same
147 chromosome as the QTL marker of interest. This leave-one-chromosome-out (LOCO) strategy
148 was chosen in order to avoid the loss of power that can arise when relatedness is computed
149 from the full complement of genotyped markers [52-54]. The LOCO approach produces a
150 unique heritability estimate for each chromosome on each PC. **Table 1** reports the mean
151 heritability for each PC, as well as the variance in these heritabilities (averaged over
152 chromosomes). For most PCs, heritability was moderately high (0.42-0.57), with a few low
153 heritability outliers. These values are very similar to those Pallares and colleagues estimated for
154 skull shape PCs in an outbred mouse sample [32], and lie mostly in the middle of the heritability
155 range for human facial shape (~30-70%) [36, 55].
156 **Table 1. Heritabilities by PC.**

| | Mean $h^2$ | Variance |
|---|---|---|
| **PC1** | 0.5407 | 0.00012 |
| **PC2** | 0.4389 | 0.00013 |
| **PC3** | 0.5418 | 0.00022 |
| **PC4** | 0.3532 | 0.00022 |
| **PC5** | 0.4627 | 0.00012 |
| **PC6** | 0.5705 | 0.00015 |
| **PC7** | 0.4785 | 0.00014 |
| **PC8** | 0.4604 | 0.00015 |
| **PC9** | 0.5411 | 0.00032 |
| **PC10** | 0.5420 | 0.00017 |
| **PC11** | 0.2439 | 0.00009 |
| **PC12** | 0.4226 | 0.00014 |
| **PC13** | 0.5309 | 0.00013 |
| **PC14** | 0.4364 | 0.00020 |
| **PC15** | 0.4849 | 0.00005 |
| **PC16** | 0.4456 | 0.00010 |
| **PC17** | 0.4658 | 0.00020 |
| **PC18** | 0.4726 | 0.00019 |
| **PC19** | 0.4533 | 0.00006 |
| **PC20** | 0.5040 | 0.00022 |

Mean and variance of heritability for PC 1-20 shape traits. The full set of heritability estimates is provided in **S2 Table**.

Based on signal-to-noise evaluation of shape PC eigenvalue decay [56], we limited further analysis to the first five PCs (effectively four PCs, as no marker exceeded the permutation significance threshold for the PC 5 shape axis). Each plot in **Fig 3** depicts the LOD score profile (lower panel) and CC founder haplotype coefficients (upper panel) for a chromosome harboring one or more QTL for a PC 1-4 shape variable. Shaded rectangular regions delimit the 1.5-LOD drop support interval boundaries for the QTL. Founder coefficients were estimated using best linear unbiased predictors [57, 58]. This helps to highlight QTL regions by imposing a degree of shrinkage on the coefficients chromosome-wide [48].

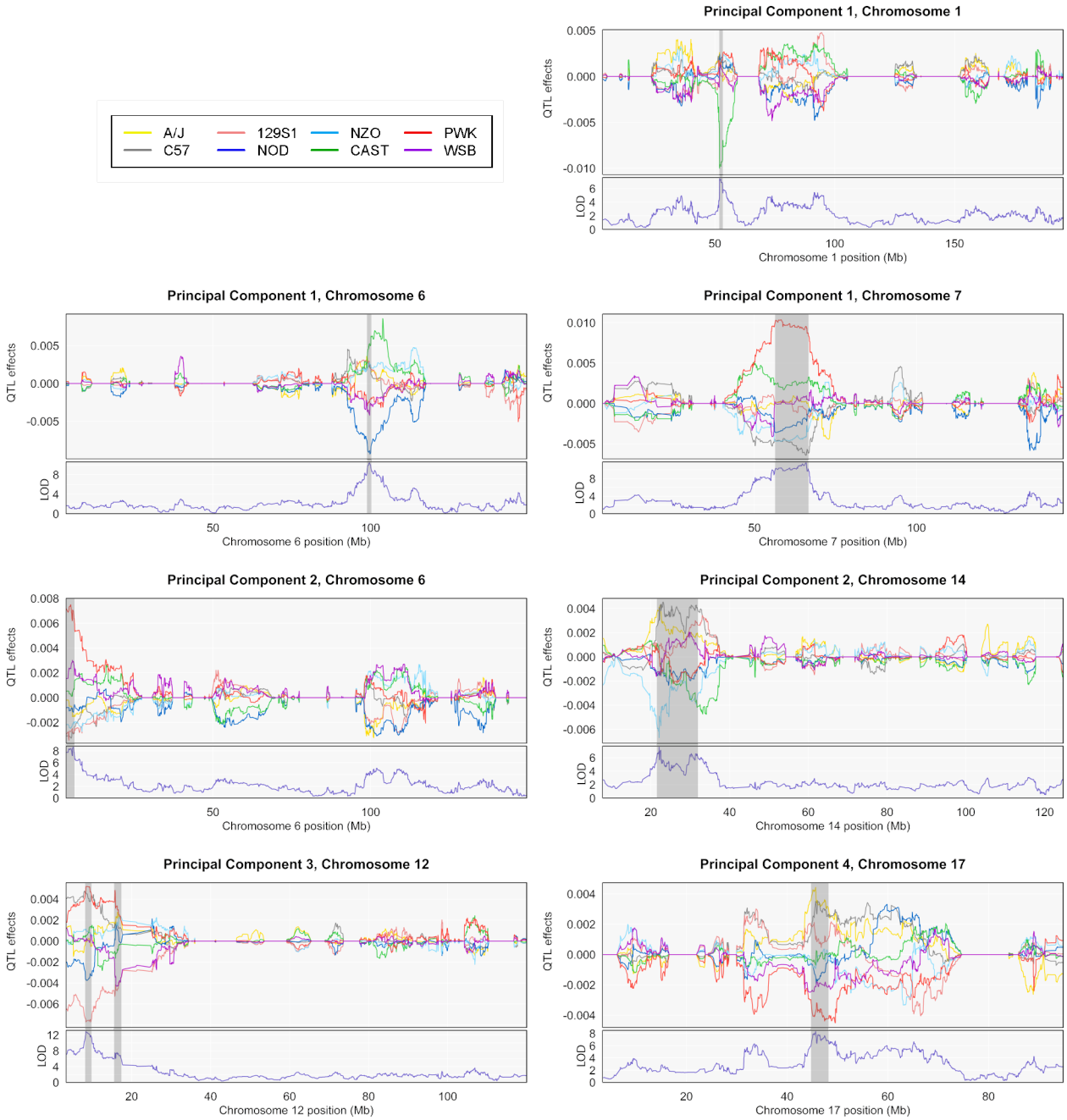


**Fig 3.** BLUP effects and LOD panels for all QTL, PCs 1-4. QTL effect colors correspond to CC founders.

We also mapped GP associations for vectors capturing covariation between shape and two measures of size: centroid size (CS) and body mass. Shape change associated CS and body mass variation were closely correlated with the primary axis of shape variation in our sample

176 ($r_{PC1\text{-}CS}$: 0.985, $r_{PC1\text{-}Mass}$: 0.875, $r_{CS\text{-}Mass}$: 0.927). These correlations carry forward to the QTL

177 profiles, as well. We identify two QTL each for CS and body mass allometry, one of which, on

178 chromosome 6, is common to the two allometry vectors. Together, the three QTL—on

179 chromosomes 1, 6, and 7—completely overlap with the PC 1 shape QTL (**Fig 4**).

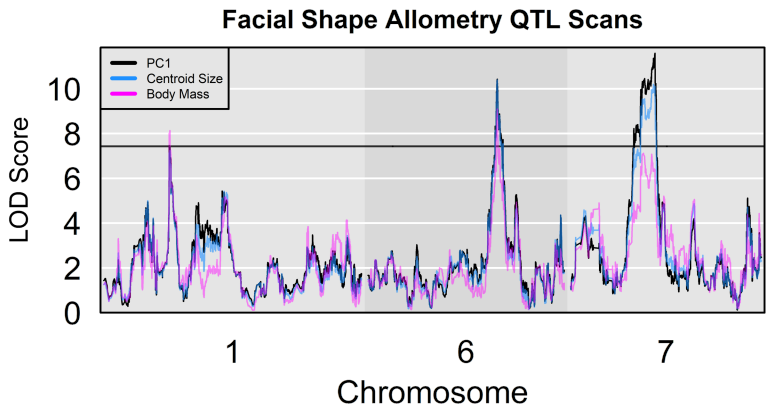


180
181 **Fig 4.** LOD plots for chromosomes containing allometry (CS and body mass) and PC 1
182 QTL. The permutation significance thresholds for all three phenotypic variables are
183 extremely similar. Only one is plotted.
184
185 The allometry results suggest a developmental model in which the determinants of

186 different size measures have partially correlated effects on cranial shape [59]. The near

187 coincidence of shape PC 1 with our explicitly allometric variables has been observed in many

188 geometric and classical morphometric investigations, and there is a long history of treating PC 1

189 as an allometry variable in morphometric analysis [59-64]. With this in mind, though primarily

190 for economy, we regard PC 1 QTL as allometry QTL in the remainder of this manuscript.

191 The mouse subspecies that comprise the CC are estimated to have diverged several

192 hundred thousand years ago [65]. In many DO studies, subspecific divergence in one or more

193 wild-derived CC lines figures prominently in the founder genetic effects contrasts that underlie

194 QTL (e.g., [66-69]). Here, the same pattern is evident for most of the PC 1-4 QTL. In six of the

195 eight QTL (or seven of nine, if the two peaks of the PC 2, chromosome 14 QTL are considered

196 distinct), the coefficient for a non-*domesticus* wild-derived strain (CAST or PWK) sits at one
197 extreme of the founder coefficient distribution. Only at the upstream LOD peak of the PC 2,
198 chromosome 14 QTL is the founder coefficient contrast clearly between *M.m. domesticus*
199 inbred lines. The prevalence of QTL substantially driven by wild-derived alleles highlights the
200 value of subspecific genetic diversity in the DO population.

201 The broad region of high LOD scores for PC 1 on chromosome 7 merits individual
202 attention. This QTL support interval essentially delimits the mouse homolog boundaries of the
203 human Prader-Willi/Angelman syndromes domain [70]. The founder coefficients point to a
204 strong subspecies signal, with PWK (*M.m. musculus*) highly differentiated from wild-derived
205 WSB and the inbred *M.m. domesticus* lines, and CAST (*M.m. castaneus*) intermediate. Though
206 the QTL interval contains fewer than 40 genes, nine are known to be imprinted [70-74]. Several
207 more have mixed evidence for imprinting [73], and Prader-Willi and Angelman are parent-of-
208 origin dependent neurological disorders [75]. In addition, more than a dozen genes in the
209 interval are expressed in the developing face [40, 76-81]. Our mapping strategy is not
210 specifically designed to quantify imprinted gene QTL [82-84]. However, closer dissection of this
211 interval's contribution to facial shape variation, accounting for allelic parent of origin effects,
212 may be warranted in the future. The characteristic facial phenotype for Prader-Willi includes a
213 relatively long skull with a narrow upper face [85]. In this regard, the shape effects associated
214 with the peak marker in this interval, just downstream of the primary Prader-Willi genes, are
215 suggestive, as they contrast a shorter, wider face with a longer, narrower one (see **Figs 5 and 6**,
216 below).

217 **Marker Effects on Shape**

218 At the LOD peak marker of each PC 1-4 QTL, we collapsed the 8-state founder
219 probabilities to 2-state SNP probabilities in order to estimate the shape effect of allelic
220 substitution at that marker. To estimate effects on total shape (instead of univariate shape
221 PCs), we employed a Bayesian mixed effects model for highly multivariate dependent
222 observations [50, 86]. The results are plotted in **Fig 5**. In each figure, QTL effects are magnified
223 by the scaling factor required to cause the QTL to account for 10% of phenotypic variance.
224 These effects are shown as displacement vectors emanating from the mean configuration
225 wireframe. The magnification ensures that even when the effect at a landmark is small, its
226 direction and relative size (in comparison to effects at other landmarks) is apparent. We further
227 exploited the Bayesian posterior to plot 80% confidence ellipsoids for the magnified
228 displacements. The actual proportion of variance explained by the SNP, without magnification,
229 is noted in the figure (and included in **Table 3**).

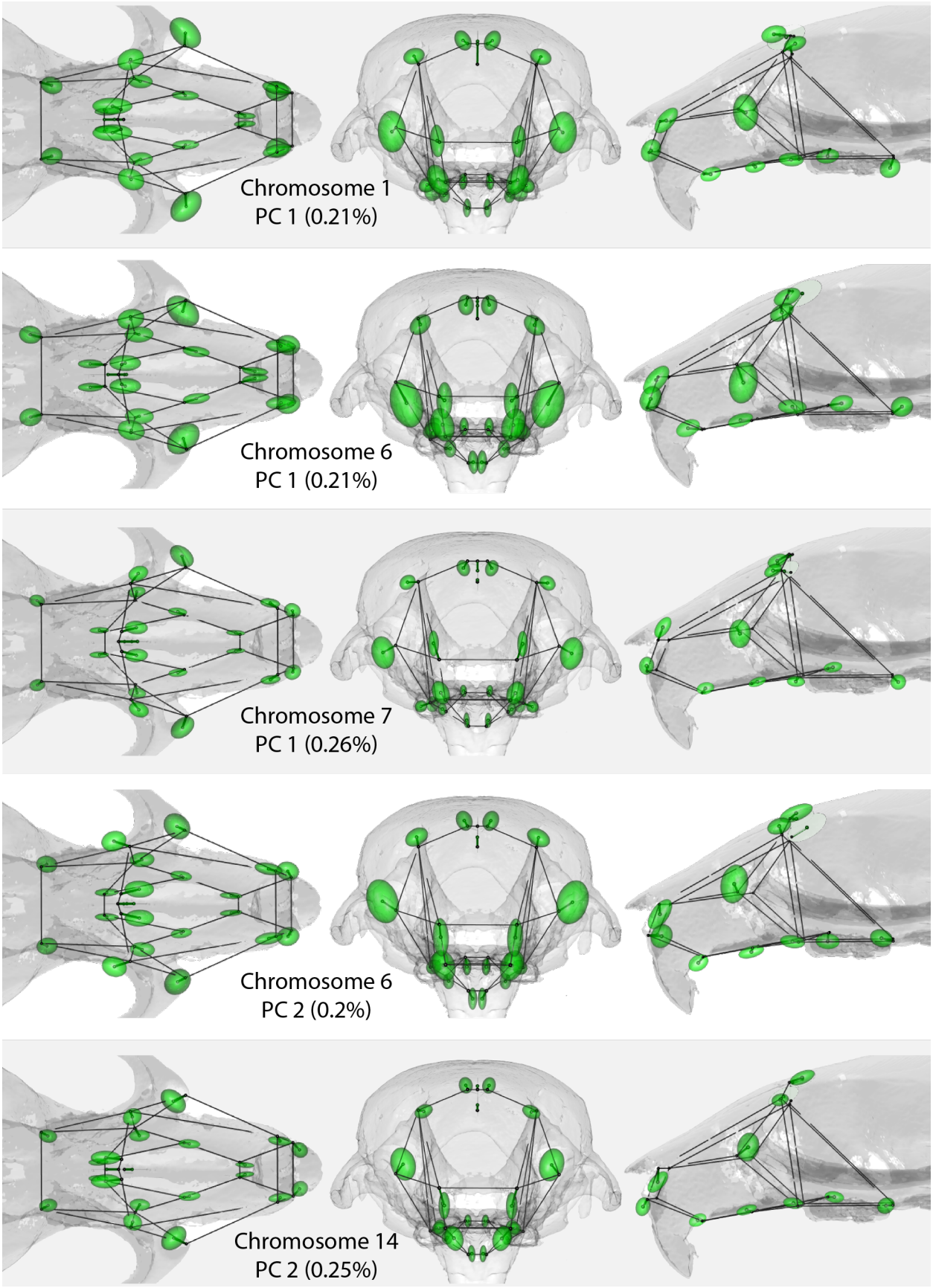
Chromosome 1
PC 1 (0.21%)
Chromosome 6
PC 1 (0.21%)
Chromosome 7
PC 1 (0.26%)
Chromosome 6
PC 2 (0.2%)
Chromosome 14
PC 2 (0.25%)

230

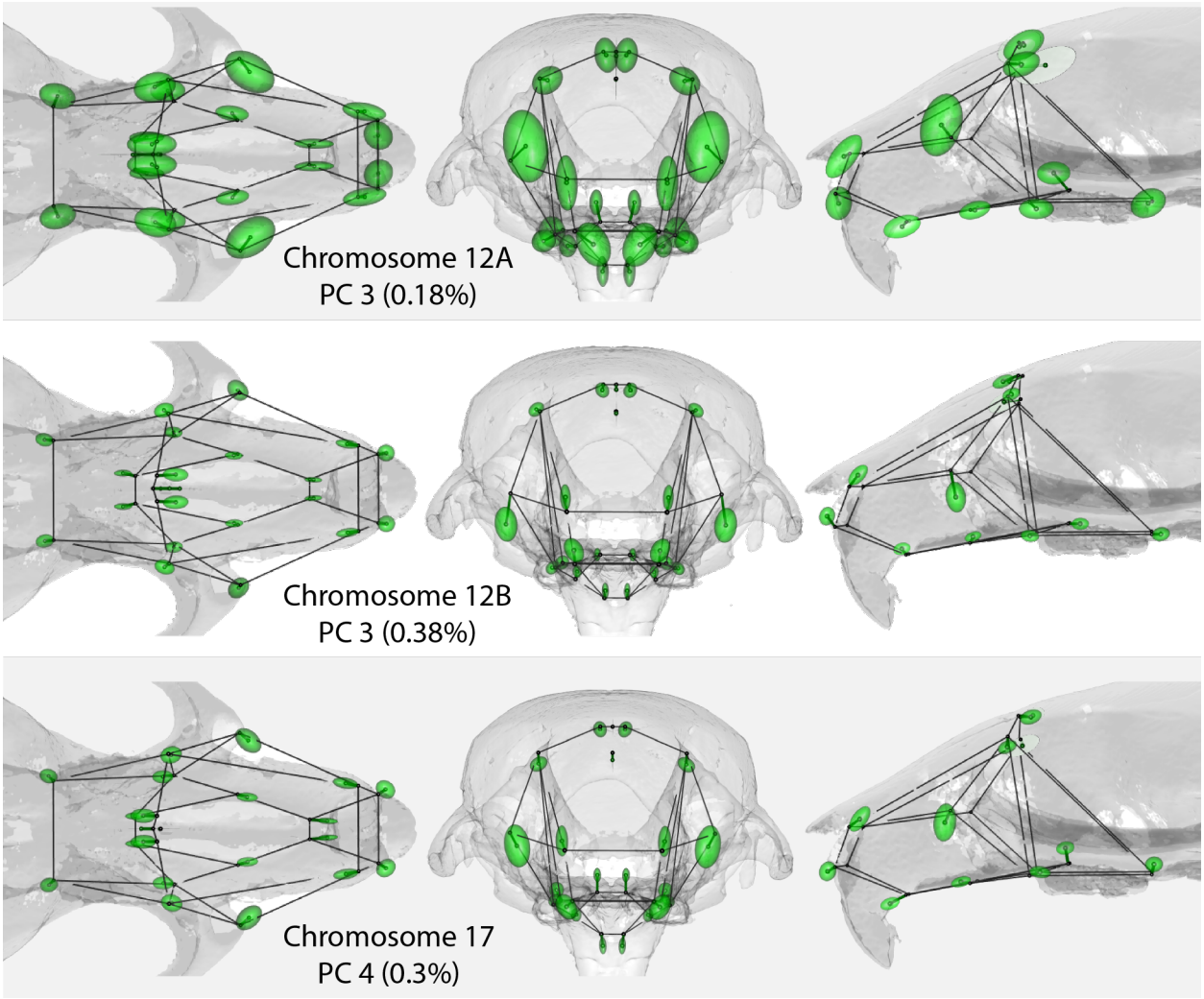


**Fig 5.** Superior (left), anterior (middle), and lateral (right) views of the (magnified) effect of allele substitution at the genome scan peak marker. Displacement vectors from wireframe to center of ellipsoids depict the mean effect. Ellipsoids enclose the approximate 80% posterior confidence boundaries.

**Biological Process Enrichment**

We used the human annotations in the online Molecular Signatures Database [87] to query biological processes relevant to craniofacial variation are overrepresented in the PC 1-4 QTL intervals. Collectively, the intervals contain 243 named, protein coding genes (**S1 File**), 232 of which are annotated in the Entrez Gene library utilized by the Molecular Signatures Database. **Table 2** provides GO biological process enrichment highlights for these intervals,

243 including FDR *q*-values adjusted for multiple testing (see **S2 File** for the top 100 *q*-value

244 processes). Growth, morphogenesis, and skeletal system development are prominent biological

245 process annotations for the facial shape QTL. The enrichment results suggest that no enriched

246 biological process is uniquely associated with shape variation on a single PC. Rather, with the

247 exception of bone development, each process in **Table 2** includes annotations to each PC.

248 **Table 2. Gene ontology enrichment for selected biological processes.**

| Biological process | FDR *q* -value | GO annotated genes |
|---|---|---|
| Animal organ morphogenesis | 1.42 e-3 | **PC1:** *Aldh1a3, Chsy1, Nab1, Stat1, Trpm1.* **PC2:** *Col1a2, Dlg5, Gngt1, Hesx1, Tnnc1, Wnt5a, Zmiz1* . **PC3:** *Gdf7, Matn3, Osr1, Sdc1.* **PC4:** *Ccdc66, Mdfi, Ptk7, Runx2, Srf, Vegfa* . |
| Growth | 2.25 e-3 | **PC1:** *Apba2, Mstn, Ndn, Nsmce3, Ube3a* . **PC2:** *Bap1, Colq, Il17rb, Mustn1, Sema3g, Tkt, Wnt5a, Zmiz1.* **PC3:** *Gdf7, Matn3, Osr1* . **PC4:** *Dnph1, Mymx, Ptk7, Srf, Taf8, Vegfa, Hsp90ab1.* |
| Skeletal system development | 1.29 e-2 | **PC1:** *Chsy1, Nab1, Foxp1, Lrrk1.* **PC2:** *Col1a2, Mustn1, Wnt5a.* **PC3:** *Matn3, Osr1, Runx2.* **PC4:** *Mdfi, Srf.* |
| Sensory organ development | 1.62 e-2 | **PC1:** *Aldh1a3, Gabra5, Gabrb3, Trpm1.* **PC2:** *Ccdc66, Gngt1, Hesx1, Wnt5a.* **PC3:** *Osr1.* **PC4:** *Prph2, Ptk7, Srf, Vegfa.* |
| Cartilage development | 2.4 e-2 | **PC1:** *Chsy1.* **PC2:** *Mustn1, Wnt5a* . **PC3:** *Matn3, Osr1.* **PC4:** *Runx2, Srf.* |
| Bone development | 2.54 e-2 | **PC1:** *Chsy1, Nab1, Lrrk1, Foxp1.* **PC3:** *Matn3.* **PC4:** *Runx2, Srf* . |

249

250 To consider annotations specific to allometric variation, we queried biological process

251 enrichment for PC 1 QTL alone (**S3 File**). Collectively, the three allometry QTL intervals were

252 significantly enriched for genes implicated in bone development (FDR $q$ = 0.025). Each of the

253 intervals included at least one such gene: *Nab1* (chromosome 1) [88], *Foxp1* (chromosome 6)

254 [89, 90], and *Lrrk1* and *Chsy1* (chromosome 7) [91-93]. The chromosome 1 interval also includes

255 Myostatin (*Mstn, Gdf8*), a negative regulator of muscle growth. Inactivation of *Mstn* has been

256 shown to greatly increase facial muscle mass, with corresponding size decreases and shape

257 changes throughout the bony face and vault [94, 95].

258 **Association Mapping**

259 Finally, to develop a finer-grained impression of potential causal loci, we performed SNP

260 association mapping within each QTL interval. We imputed a dense map of SNP probabilities to

261 the sample by inferring their bi-allelic (major/minor) probabilities based on (a) founder

262 probabilities at flanking, genotyped markers and (b) major/minor strain distribution patterns in

263 the CC founder variants **(Fig 6)**.

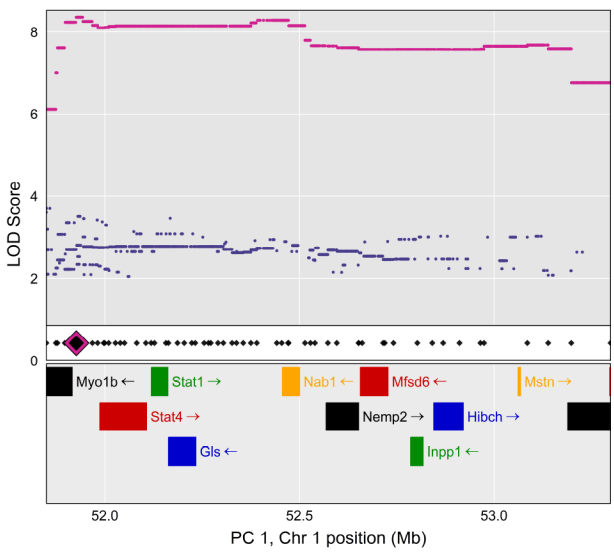
LOD Score
Myo1b ←
Stat1 →
Nab1 ←
Mfsd6 ←
Mstn →
Stat4 →
Nemp2 →
Hibch →
Gls ←
Inpp1 ←
PC 1, Chr 1 position (Mb)

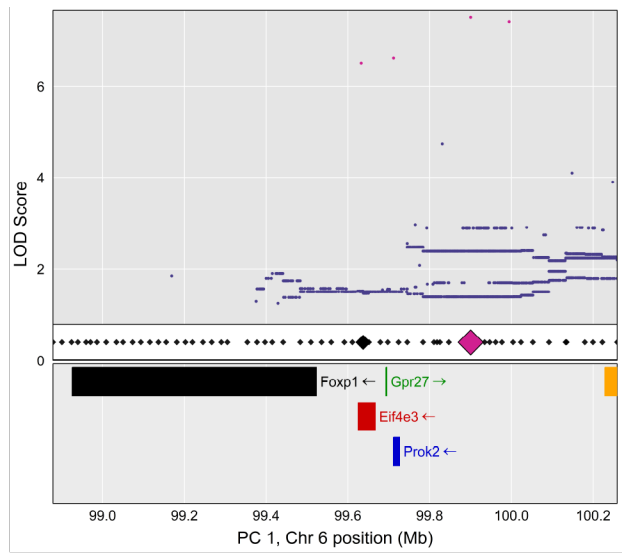
LOD Score
Foxp1 ←
Gpr27 →
Eif4e3 ←
Prok2 ←
PC 1, Chr 6 position (Mb)

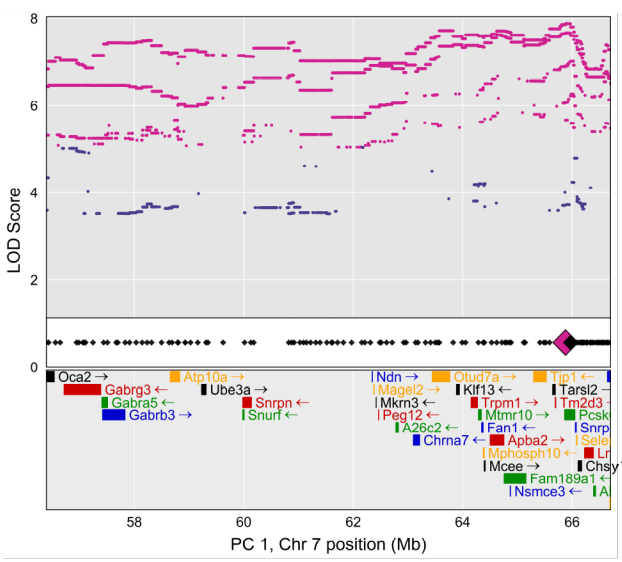
LOD Score
Oca2 →
Atp10a →
Gabrg3 ←
Ube3a →
Gabra5 ←
Snrpn ←
Gabrb3 →
Snurf ←
Ndn →
Otud7a →
Tip1 ←
Magel2 →
Klf13 ←
Tarsl2 →
Mkrn3 ←
Trpm1 →
Tm2d3 →
Peg12 ←
Mtmr10 →
Pcsk
A26c2 ←
Fan1 ←
Snrp
Chrna7 ←
Apba2 →
Sele
Mphosph10 ←
Lr
Mcee →
Chsy1
Fam189a1 ←
Nsmce3 ←
PC 1, Chr 7 position (Mb)

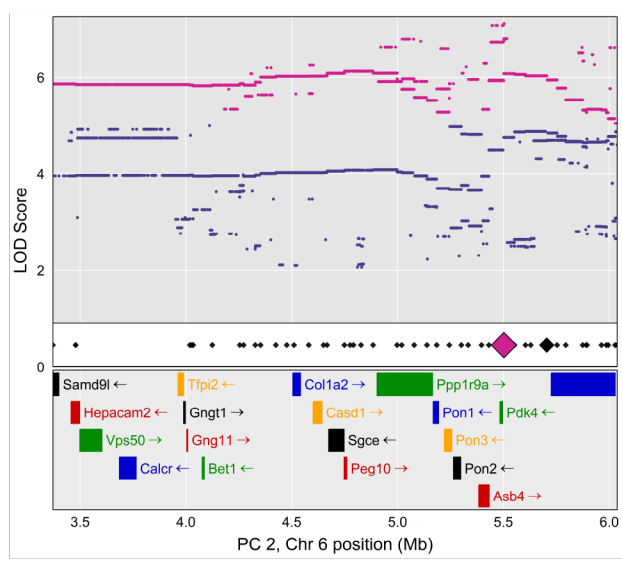
LOD Score
Samd9l ←
Tfpi2 ←
Col1a2 →
Ppp1r9a →
Hepacam2 ←
Gngt1 →
Casd1 →
Pon1 ←
Pdk4 ←
Vps50 →
Gng11 →
Sgce ←
Pon3 ←
Calcr ←
Bet1 ←
Peg10 →
Pon2 ←
Asb4 →
PC 2, Chr 6 position (Mb)

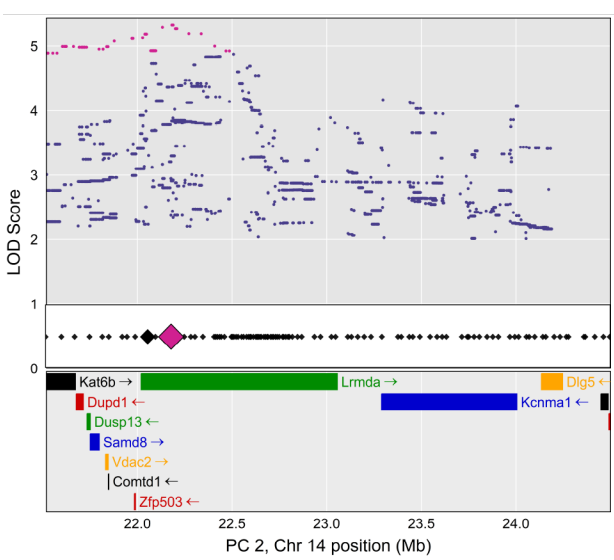
LOD Score
Kat6b →
Lrmda →
Dlg5 ←
Dupd1 ←
Kcnma1 ←
Dusp13 ←
Samd8 →
Vdac2 →
Comtd1 ←
Zfp503 ←
PC 2, Chr 14 position (Mb)

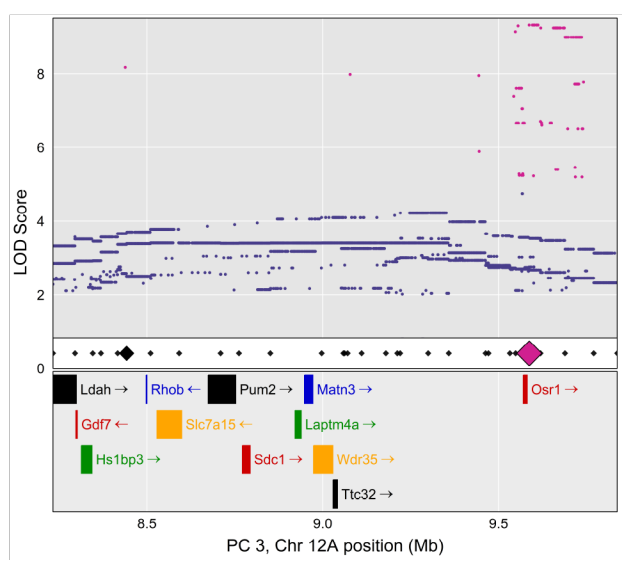
LOD Score
Ldah →
Rhob ←
Pum2 →
Matn3 →
Osr1 →
Gdf7 ←
Slc7a15 ←
Laptm4a →
Hs1bp3 →
Sdc1 →
Wdr35 →
Ttc32 →
PC 3, Chr 12A position (Mb)

264

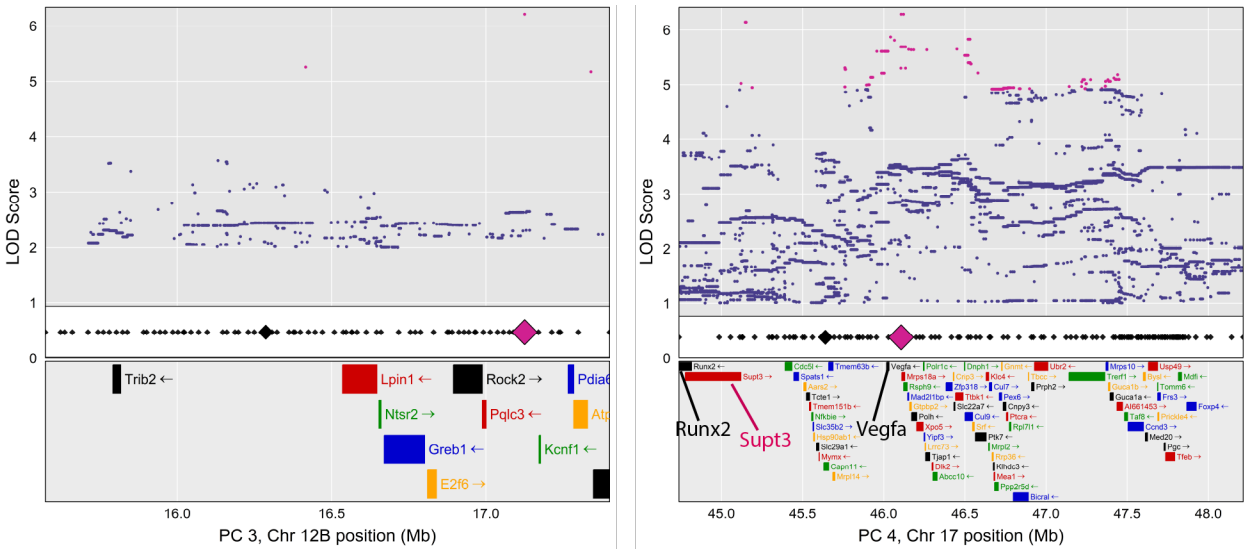


**Fig 6.** Association mapping results for PC 1-4 QTL intervals. Top panels: LOD scores for all CC SNP variants in the interval. Magenta points are locations where inferred bi-allelic SNP probabilities (based on strain distribution patterns in the CC) exceed the 95% LOD threshold. To control file size, low LOD scores points have been omitted from most plots. Middle panel: location of genotyped markers in the DO (small black diamonds), highlighting LOD peak locations for the founder genome scan (large black diamond) and SNP association scan (large magenta diamond). Bottom panel: named, protein coding genes for intervals. For legibility, we show the portion of the PC 2, Chromosome 14 map that contains both peak LOD scores and all SNPs exceeding the LOD threshold. For all plots, the complete gene list is provided in **S1 File**.

We then queried whether any genes within 0.25 Mb of the SNP or genome scan LOD peaks are known to be associated with craniofacial development or phenotypes **(Table 3)**. As with human facial shape GWAS [42], LOD peaks tended to be located in non-coding regions. While the focal genes we identified all have known roles in skeletal or craniofacial development, they also tend to be developmentally ubiquitous. *Stat1* (PC1, chr. 1) is implicated in bone development and remodeling throughout life [96-98]. Overexpression of *Foxp1* (PC1, chr. 6) can attenuate osteoblast differentiation, chondrocyte hypertrophy, osteoclastogenesis, and bone resorption, while *Foxp1* deficiency can accelerate ossification [89, 90]. In humans, some *Foxp1* mutations produce a facial phenotype that includes broad forehead and short nose

286 [99]. Chondrogenesis is generally disrupted in *Chsy1* null mouse mutants (PC1, chr. 7), and in
287 humans, *Chsy1* mutations can manifest in micrognathia and short stature [92, 100]. *Kat6b* (PC2,
288 Chr. 14) activates the transcription factor *Runx2*, which is often referred to as a master
289 regulator of bone formation [101-103]. For the PC3 QTL at 8.23 – 9.84 Mb on chromosome 12,
290 the founder and SNP LOD peaks reside at opposite ends of the QTL interval, but each is very
291 close to an important craniofacial development gene: *Gdf7* (*Bmp12*) contributes to patterning
292 of the jaw joint and is expressed in the developing incisor pulp and periodontium [104-106];
293 *Osr1* is broadly expressed in the embryonic and developing skull, with overexpression resulting
294 in intramembranous ossification deficiencies, increased chondrocyte differentiation, and
295 incomplete suture closure, while under-expression may contribute to cleft palate phenotype
296 [107-109]. *Osr1* has also previously been identified as a candidate in human facial shape GWAS
297 [23]. Finally, the SNP LOD peak for PC4, chromosome 17 implicates *Vegfa*, which is critical to
298 endochondral and intramembranous ossification through its role in angiogenesis [110]. A
299 distinct SNP LOD peak of nearly equal magnitude is located approximately 1 Mb upstream (at
300 rs47194347), very close to *Supt3* (human ortholog *Supt3h*) and *Runx2*. In addition to the central
301 role *Runx2* has in bone formation and development [102], both genes are human facial shape
302 GWAS candidates [15, 22].
303 **Table 3. Candidate genes.**

| PC | Chr | Founder Peak (Mb) | Founder ID | Founder type | SNP Peak (Mb) | SNP ID | SNP_type | SNP % Var | Candidates |
|---|---|---|---|---|---|---|---|---|---|
| PC1 | 1 | 51.926616 | rs48415864 | intergenic | 51.926623 | rs254750887 | intergenic | 0.21 | *STAT1* |
| PC1 | 6 | 99.637221 | rs226005706 | intron | 99.900271 | rs31234872 | intergenic | 0.21 | *FOXP1* |
| PC1 | 7 | 65.970847 | rs33905059 | intron | 65.876674 | rs32405988 | intron | 0.26 | *CHSY1* |
| PC2 | 6 | 5.704731 | rs49620919 | intergenic | 5.502445 | rs32485785 | intergenic | 0.2 | NA |
| PC2 | 14 | 22.058402 | rs30739483 | intron | 22.182166 | rs30740474 | intron | 0.25 | *KAT6B* |
| PC3 | 12 | 8.44203 | rs48833407 | intergenic | 9.587123 | rs29212735 | intergenic | 0.18 | *OSR1, GDF7* |
| PC3 | 12 | 16.286802 | rs49949506 | intergenic | 17.125642 | SV 17121898: 17129386 | structural (deletion) | 0.38 | NA |
| PC4 | 17 | 45.639772 | rs107675960 | intron | 46.106749 | rs108721614 | upstream gene variant | 0.3 | *VEGFA [RUNX2, SUPT3]* |

Candidate genes located within 0.25 Mb of founder or SNP QTL peaks. SNP % Var gives the percentage of variation explained by substitution of an additional reference allele at the founder (genome scan) peak.

While GP maps for traits influenced by many genes may be quite intricate and layered, additive effect QTL analyses remain an indispensable means to identify loci that contribute to phenotypic variation. Our investigation advances understanding of the genetics of facial skeletal diversity in several ways. The 37 QTL identified herein substantially expand the small but growing facial shape QTL library. Compared to similar prior studies, the number of QTL is relatively large and their confidence intervals relatively narrow. These results affirm the value of larger samples, sophisticated animal models like the outcrossed population utilized here, and high-resolution genotyping for identification and localization of QTL. Synthesizing our results with prior insights from developmental biology and medical genetics provides a richer picture of the sources of facial skeletal diversity. We found a relative abundance of skeletal and craniofacial development genes in QTL intervals for the largest shape PCs. Moreover, these genes tend to be located very close to QTL peaks. Thus, our results suggest that genes essential to building a face are often also the genes that cause faces to vary. Finally, QTL effect sizes were small. In summary, our results are consistent with a model of facial diversity that is influenced by key genes in skeletal and facial development and, simultaneously, highly polygenic.

324 ## Materials and methods

325 **Diversity Outbred mouse population**

326 The DO (Jackson Laboratory, www.jax.org) are derived from the eight inbred founder
327 lines that contribute to the CC [43, 44], which include three mouse subspecies, and both wild-
328 derived and laboratory strains [46]. Continued random outcrossing of the DO has produced a
329 population with relatively high genetic diversity (~45 million SNPs segregating in the CC
330 founding populations [43]) and increasingly fine mapping resolution in advancing generations.
331 In combination, these features increase the potential to identify multiple QTL for
332 complex traits [31]. On average, the genomes of the eight CC founders should be equally
333 represented in the DNA of any DO animal. Sequenced genomes for the CC make it possible to
334 characterize and interpret genetic variants in the DO according to 8-state founder identity and
335 as bi-allelic (major/minor allele) SNP variation. In addition, statistical packages designed for
336 analysis of the DO offer features to impute variants at each typed SNP in the CC founders, using
337 the coarser DO marker map as a scaffold to infer a high-density SNP map.

338 **Computing**

339 All analysis was conducted in R [111]. Customized data processing and statistical analysis
340 functions for mapping experiments in DO samples were originally published in the DOQTL
341 package [49]. These routines are now incorporated into the qlt2 package [48], with additional
342 processing and genotype diagnostic tools provided at https://kbroman.org/qtl2/.

343 **Images, landmark data**

344 Our DO sample consists of *n*=1147 male and female adult mice (after exclusion of some
345 records; see *Genotypes*, below) from seven DO generations (**Table 4**). We obtained µCT images

346 of the mouse skulls in the 3D Morphometrics Centre at the University of Calgary on a Scanco
347 vivaCT40 scanner (Scanco Medical, Brüttisellen, Switzerland) at 0.035 mm voxel dimensions at
348 55kV and 72-145 µA. On each skull, one of us (WL) collected 54 3D landmark coordinates from
349 minimum threshold-defined bone surface with ANALYZE 3D (www.mayo.edu/bir/). Here, we
350 analyzed the 22-landmark subset of the full configuration—a 66 coordinate dimension vector—
351 that captures the shape of the face (**Fig 1**).

352 **Table 4. DO sample composition.**

| | DO generation | | | | | | |
|---|---|---|---|---|---|---|---|
| | **9** | **10** | **15** | **19** | **21** | **23** | **27** |
| **Female** | 91 | 221 | 80 | 55 | 80 | 97 | 75 |
| **Male** | 0 | 144 | 0 | 58 | 77 | 99 | 70 |
| **MUGA Array** | Mega | Mega | Mega | Giga | Giga | Giga | Giga |

353
354 Overview of the DO sample by generation, sex, and genotyping array.
355
356 **Ethics Statement**

357 No animals were sacrificed for this study. Specimens were raised in several labs for
358 unrelated experiments under approval and conduced in accordance with the guidelines set
359 forth by the Institutional Animal Care and Use Committee in accordance with protocols #11-299
360 (University of North Carolina Chapel Hill), #99066 and #15026 (Jackson Labs), and #08-0150-3
361 (Scripps Research Institute). Receipt of animal carcasses and micro-CT (µCT) imaging of mouse
362 skulls were undertaken in accordance with approved IACUC protocol #AC18-0026 at the
363 University of Calgary.

364 **Shape data**

365 Landmark configurations were symmetrically superimposed by Generalized Procrustes
366 Analysis (GPA) [112] using the Morpho package [113]. GPA is a multi-step procedure that
367 removes location and centroid size differences between configurations, then (iteratively)

368 rotates each configuration to minimize its squared distance from the sample mean. We chose a
369 superimposition that decomposes shape variation into its symmetric and asymmetric
370 components [114, 115], and stored the symmetric configurations for analysis. Working with
371 symmetric, superimposed data reduced morphological degrees of freedom from 66 landmark
372 coordinate dimensions to 30 shape dimensions [115].

373 **Genotypes**

374 For all animals, DNA was extracted from ear or tail clippings. Genotyping was performed
375 by the Geneseek operations of Neogen Corp. (Lincoln, NE). Mice from generations 9, 10, and 15
376 were genotyped using the MegaMUGA genotyping array (77,808 markers); mice from
377 generations 19, 21, 23, and 27 were genotyped using the larger GigaMUGA array (143,259
378 markers) [116]. The two arrays share 58,907 markers in common. We restricted the genotype
379 data to these shared SNPs [116].

380 In addition, we excluded 2,022 markers from the center of chromosome 2 (40 - 140
381 Mb). WSB alleles are highly overrepresented in this genomic region in earlier DO generations.
382 This overrepresentation has been attributed to female meiotic drive favoring WSB at the *R2d2*
383 locus [117]. Between DO generations 12 and 21, Jackson Labs systematically purged the meiotic
384 drive locus and linked effects from the DO [45]. Our samples closely track this history, with WSB
385 allele frequencies in the middle of chromosome 2 exceeding 60% in generation 9 and falling to
386 0% by generation 23 (**S2 Fig**). If unaddressed, this directional shift in allele frequencies can
387 confound statistical analysis of genotype-phenotype associations [118] with potentially false
388 positive associations between WSB chromosome 2 haplotypes and directional changes in
389 phenotype over DO generations. After removing this genomic region from consideration, the

390 final SNP dataset consists of 56,885 markers common to the MegaMUGA and GigaMUGA
391 arrays, with a mean spacing of 48 kb.
392 The qtl2 package estimates genotype probabilities, including imputation of sporadically
393 missing genotypes, with a multipoint Hidden Markov Model (HMM) on the observed marker
394 genotypes. From these initial genotype probabilities, we derived three probabilistic
395 representations of genetic state for each observation at each marker: (1) for genome scans,
396 founder probabilities, a vector encoding the probability of genetic contribution from each of
397 the eight CC founders to the diplotype state; (2) for association mapping, SNP probabilities,
398 collapsing the eight founder probabilities to a two-state, major/minor allele strain distribution;
399 and (3) for mapping multivariate shape effects, additive SNP dosage, twice the estimated major
400 SNP probability (maximum additive SNP dosage = 2).
401 We identified problematic genetic samples using the DO genotype diagnostics tools
402 available at https://kbroman.org/qtl2/ [119]. A total of 11 observations were excluded due to
403 excessive missing marker data, which we defined as no marker information at >7.5% of
404 markers. Three probable duplicate sets of genetic data (>99% of markers identical) were
405 identified. Because the correct genotype-phenotype matches could not be established by other
406 evidence, all six animals were removed from the sample. Finally, we excluded seven female
407 samples with low X chromosome array intensity values. These samples are potentially XO [45],
408 which can affect facial form and body size [120, 121]. The exclusions described above resulted
409 in a final, retained sample of $n$ = 1147 animals.
410 **Genome scan and association mapping**

411 We mapped QTL for facial shape and facial shape allometry. To identify QTL, we
412 implemented the linear mixed effects regression model in qtl2. The qtl2 genome scan is
413 designed to estimate marker effects on one or more univariate observations, but not
414 covariance among those dimensions. We therefore decomposed the superimposed coordinates
415 into PCs, treating the specimen scores on each PC as measured traits. For allometry, we treated
416 common allometric component scores [61] as measured traits. Prior to deriving PCs and
417 allometry vectors, we centered each observation on its generation mean in order to focus on
418 shared, within-generation covariance patterns [122, p. 295].
419 At each marker, we fit a mixed model with fixed effect coefficients for sex, age-at-
420 sacrifice, and the additive effect of each CC founder haplotype, a random effect of kinship, and
421 an error term [49]. Evidence for a QTL was evaluated based on marker LOD scores, likelihood
422 ratios comparing the residuals of the marker model to a null model excluding the marker's
423 effect [51]. We consider the evidence for a marker-phenotype association to be statistically
424 significant where the LOD score exceeds the 95% quantile of genome-wide maximum LOD
425 scores computed from 1000 random permutations of genotype-phenotype associations [123].
426 We use a 1.5 LOD-drop rule to define the boundaries of QTL support intervals [124], and allow
427 for multiple QTL peaks on a single chromosome.
428 The random effect of kinship depends upon pairwise proportions of shared alleles
429 among observations, encoded in a kinship matrix. Loss of power to detect QTL can arise when
430 the marker of interest and linked genes are included in the kinship matrix of the null model. To
431 avoid this problem, we compute kinship matrices using a leave-one-chromosome-out (LOCO)
432 approach [52-54].

433 Genome scans, QTL support intervals, and proportions of shape variation attributable to
434 founder-level kinship (heritability) were estimated for all PCs explaining more than 1% of
435 symmetric shape variation. However, we limit more in-depth analysis to the five PCs with
436 reasonably large signal-to-noise ratios (**S2 Fig**). This was assessed using the modified "noise
437 floor" detection strategy developed by Marroig and colleagues in [56].
438 In addition, within the PC 1-5 QTL intervals, we used a form of merge analysis to
439 perform genome-wide association mapping [49, 125, 126]. For each CC founder variant located
440 between a flanking pair of genotyped markers, the vector of founder allele probabilities is
441 assumed to be the average of the founder probabilities at those flanking markers. The bi-allelic
442 SNP probabilities were computed from these founder probabilities and the major/minor allele
443 strain distribution pattern in the CC. Analysis was again via mixed effects regression model, with
444 the imputed SNP data as genotype predictors.

445 **Enrichment analysis and candidate genes**

446 Modern GWAS and QTL studies often attempt to contextualize QTL and candidate gene
447 results post hoc via GO enrichment analysis. Given a list of genes near statistically significant
448 markers, a GO analysis calculates the probability that a random set of genes of the same size
449 would contain as many genes under a common annotation term, typically after a family-wise
450 error rate or FDR adjustment for multiple testing. The outcome of enrichment analysis is a list
451 of GO terms (or in the absence of any enrichment, no list), which provides a means to consider
452 whether certain biological processes, cellular components, or molecular functions are over-
453 represented in the list of genes [127].

454 For protein coding genes in the PC 1-5 QTL support intervals and for allometry QTL, we
455 used the Molecular Signatures Database [87] online tool and Entrez Gene library [128] to
456 identify biological process GO term enrichment [129]. The database application implements a
457 hypergeometric test of statistical significance, quantifying the probability of sampling, without
458 replacement, as many (*k*) or more genes annotated to a GO term, given the total number of
459 genes annotated to that term (*K*) and the number of genes in the QTL and Entrez gene sets (*n*
460 and *N,* respectively). For each ontology term, after adjustment for multiple testing, we required
461 a FDR *q*-value < 0.05 to conclude that there was substantial evidence for GO biological process
462 enrichment. We also inspected the association mapping results in the +/- 0.25 Mb region
463 centered at each LOD peak for genes with convincing evidence of a role in skeletal, craniofacial,
464 or dental development or disease. For most QTL, LOD peaks for the genome scan and
465 association mapping results are virtually coincident. Where they differ substantially, we
466 examine the region around both peaks.

467 **Marker effects on shape**

468 We considered a significant association between a marker and facial shape along a PC
469 axis to be evidence of some effect on the multivariate (undecomposed) shape coordinate data.
470 In order to obtain an estimate of the full shape effect, we fit an additional mixed model for the
471 maximum LOD score marker. Fitting a mixed model for highly multivariate data presents a
472 significant computational challenge because the number of parameters that must be estimated
473 for the random effects covariance matrix scales quadratically with the number of traits (here,
474 465 parameters for 30 free variables). To address this challenge, we estimated mixed model
475 covariance matrices using a Bayesian sparse factorization approach [50, 86, 130]. After a

476 1,000,000 iteration burn-in, we generated 1,000,000 realizations from a single Markov chain,
477 thinning at a rate of 1,000 to store 1,000 posterior samples for inference. Though the time
478 needed to fit such a model makes it impractical for a genome scan on a dense array, it is a
479 useful strategy for disentangling kinship from the effect on multivariate outcomes at a small
480 number of peak markers. For these regressions, the marker effect predictor was twice the
481 major SNP probability. Thus, the multivariate mixed model we implemented estimates an
482 average effect of allele substitution, a standard quantity in quantitative genetics [131]. In
483 addition, for each regression, we estimated the proportion of shape variation explained using a
484 version of the coefficient of determination ($R^2$) that has been adapted for mixed model
485 parameters [132].

486 When plotting shape effects, we magnify the allele substitution coefficients by the
487 scaling factor needed to cause the QTL to explain 5% of phenotypic variance. This magnification
488 is applied both to the mean effect, in order to depict the mean displacement vector, and to the
489 posterior distribution of effects, in order to depict confidence ellipsoids. Ellipsoids were
490 estimated with the 3D ellipse function in the R package rgl [133]. While it is more typical to use
491 a 95% support boundary to evaluate effect uncertainty, with shape data, morphological
492 contrasts are best understood over the configuration as a whole [134]. The 80% ellipsoids are
493 meant to encourage this perspective.

494

495 **Acknowledgements**

496 Thanks to Xiang Zhao for help with preparation of samples and David Eby for helpful
497 intervention with the online Molecular Signatures Database. We thank Kunjie Hua, Liyang Zhao

and Kuo-Chen Jung for assistance with UNC mouse experiments. Charles Farber is gratefully acknowledged for assistance with processing of UNC mouse carcasses. All UNC mouse procedures were approved and guided by the appropriate institutional animal ethics committees, including the University of North Carolina at Chapel Hill.

## REFERENCES

1. Hu D, Marcucio RS. A SHH-responsive signaling center in the forebrain regulates craniofacial morphogenesis via the facial ectoderm. Development. 2009;136(1):107-16. Epub 2008/11/26. doi: 10.1242/dev.026583. PubMed PMID: 19036802; PubMed Central PMCID: PMCPMC2685963.
2. Hallgrímsson B, Jamniczky H, Young NM, Rolian C, Parsons TE, Boughner JC, et al. Deciphering the palimpsest: studying the relationship between morphological integration and phenotypic covariation. Evolutionary Biology. 2009;36(4):355-76.
3. Hallgrimsson B, Mio W, Marcucio RS, Spritz R. Let's face it--complex traits are just not that simple. PLoS Genet. 2014;10(11):e1004724. Epub 2014/11/06. doi: 10.1371/journal.pgen.1004724. PubMed PMID: 25375250; PubMed Central PMCID: PMCPMC4222688.
4. Varón-González C, Pallares LF, Debat V, Navarro N. Mouse Skull Mean Shape and Shape Robustness Rely on Different Genetic Architectures and Different Loci. Front Genet. 2019;10:64. Epub 2019/02/12. doi: 10.3389/fgene.2019.00064. PubMed PMID: 30809244; PubMed Central PMCID: PMCPMC6379267.
5. Young NM, Chong HJ, Hu D, Hallgrímsson B, Marcucio RS. Quantitative analyses link modulation of sonic hedgehog signaling to continuous variation in facial growth and shape. Development. 2010;137(20):3405-9. Epub 2010/09/08. doi: 10.1242/dev.052340. PubMed PMID: 20826528; PubMed Central PMCID: PMCPMC2947484.
6. Green RM, Fish JL, Young NM, Smith FJ, Roberts B, Dolan K, et al. Developmental nonlinearity drives phenotypic robustness. Nat Commun. 2017;8(1):1970. Epub 2017/12/06. doi: 10.1038/s41467-017-02037-7. PubMed PMID: 29213092; PubMed Central PMCID: PMCPMC5719035.
7. Mitteroecker P, Bookstein F. The Conceptual and Statistical Relationship between Modularity and Morphological Integration. Systematic Biology. 2007;56(5):818-36. doi: 10.1080/10635150701648029.
8. Szabo-Rogers HL, Smithers LE, Yakob W, Liu KJ. New directions in craniofacial morphogenesis. Dev Biol. 2010;341(1):84-94. Epub 2009/11/24. doi: 10.1016/j.ydbio.2009.11.021. PubMed PMID: 19941846.
9. Francis-West P, Crespo-Enriquez I. Vertebrate Embryo: Craniofacial Development. eLS [Internet]. 2016:[1-15 pp.].

10. Falconer DS, Mackay TF. Introduction to quantitative genetics. 4th ed. Essex: Pearson Education Limited; 2009.
11. Huang W, Mackay TF. The Genetic Architecture of Quantitative Traits Cannot Be Inferred from Variance Component Analysis. PLoS Genet. 2016;12(11):e1006421. Epub 2016/11/03. doi: 10.1371/journal.pgen.1006421. PubMed PMID: 27812106; PubMed Central PMCID: PMCPMC5094750.
12. Barton NH, Keightley PD. Understanding quantitative genetic variation. Nat Rev Genet. 2002;3(1):11-21. doi: 10.1038/nrg700. PubMed PMID: 11823787.
13. Varón-González C, Navarro N. Epistasis regulates the developmental stability of the mouse craniofacial shape. Heredity (Edinb). 2019;122(5):501-12. Epub 2018/09/12. doi: 10.1038/s41437-018-0140-8. PubMed PMID: 30209292; PubMed Central PMCID: PMCPMC6461946.
14. Wolf JB, Leamy LJ, Routman EJ, Cheverud JM. Epistatic pleiotropy and the genetic architecture of covariation within early and late-developing skull trait complexes in mice. Genetics. 2005;171(2):683-94. Epub 2005/07/14. doi: 10.1534/genetics.104.038885. PubMed PMID: 16020793; PubMed Central PMCID: PMCPMC1456798.
15. Claes P, Roosenboom J, White JD, Swigut T, Sero D, Li J, et al. Genome-wide mapping of global-to-local genetic effects on human facial shape. Nat Genet. 2018;50(3):414-23. Epub 2018/02/19. doi: 10.1038/s41588-018-0057-4. PubMed PMID: 29459680; PubMed Central PMCID: PMCPMC5937280.
16. Lee MK, Shaffer JR, Leslie EJ, Orlova E, Carlson JC, Feingold E, et al. Genome-wide association study of facial morphology reveals novel associations with FREM1 and PARK2. PLoS One. 2017;12(4):e0176566. Epub 2017/04/25. doi: 10.1371/journal.pone.0176566. PubMed PMID: 28441456; PubMed Central PMCID: PMCPMC5404842.
17. Liu F, van der Lijn F, Schurmann C, Zhu G, Chakravarty MM, Hysi PG, et al. A genome-wide association study identifies five loci influencing facial morphology in Europeans. PLoS Genet. 2012;8(9):e1002932. Epub 2012/09/13. doi: 10.1371/journal.pgen.1002932. PubMed PMID: 23028347; PubMed Central PMCID: PMCPMC3441666.
18. Paternoster L, Zhurov AI, Toma AM, Kemp JP, St Pourcain B, Timpson NJ, et al. Genome-wide association study of three-dimensional facial morphology identifies a variant in PAX3 associated with nasion position. Am J Hum Genet. 2012;90(3):478-85. Epub 2012/02/16. doi: 10.1016/j.ajhg.2011.12.021. PubMed PMID: 22341974; PubMed Central PMCID: PMCPMC3309180.
19. Shaffer JR, Orlova E, Lee MK, Leslie EJ, Raffensperger ZD, Heike CL, et al. Genome-Wide Association Study Reveals Multiple Loci Influencing Normal Human Facial Morphology. PLoS Genet. 2016;12(8):e1006149. Epub 2016/08/25. doi: 10.1371/journal.pgen.1006149. PubMed PMID: 27560520; PubMed Central PMCID: PMCPMC4999139.
20. Crouch DJM, Winney B, Koppen WP, Christmas WJ, Hutnik K, Day T, et al. Genetics of the human face: Identification of large-effect single gene variants. Proc Natl Acad Sci U S A. 2018;115(4):E676-E85. Epub 2018/01/04. doi: 10.1073/pnas.1708207114. PubMed PMID: 29301965; PubMed Central PMCID: PMCPMC5789906.
21. Cole JB, Manyama M, Kimwaga E, Mathayo J, Larson JR, Liberton DK, et al. Genomewide Association Study of African Children Identifies Association of SCHIP1 and PDE8A with Facial Size and Shape. PLoS Genet. 2016;12(8):e1006174. Epub 2016/08/25. doi:

579 10.1371/journal.pgen.1006174. PubMed PMID: 27560698; PubMed Central PMCID:
580 PMCPMC4999243.
581 22. Adhikari K, Fuentes-Guajardo M, Quinto-Sánchez M, Mendoza-Revilla J, Camilo Chacón-
582 Duque J, Acuña-Alonzo V, et al. A genome-wide association scan implicates DCHS2, RUNX2,
583 GLI3, PAX1 and EDAR in human facial variation. Nat Commun. 2016;7:11616. Epub 2016/05/19.
584 doi: 10.1038/ncomms11616. PubMed PMID: 27193062; PubMed Central PMCID:
585 PMCPMC4874031.
586 23. Cha S, Lim JE, Park AY, Do JH, Lee SW, Shin C, et al. Identification of five novel genetic
587 loci related to facial morphology by genome-wide association studies. BMC Genomics.
588 2018;19(1):481. Epub 2018/06/19. doi: 10.1186/s12864-018-4865-9. PubMed PMID: 29921221;
589 PubMed Central PMCID: PMCPMC6008943.
590 24. Richmond S, Howe LJ, Lewis S, Stergiakouli E, Zhurov A. Facial Genetics: A Brief
591 Overview. Front Genet. 2018;9:462. Epub 2018/10/16. doi: 10.3389/fgene.2018.00462.
592 PubMed PMID: 30386375; PubMed Central PMCID: PMCPMC6198798.
593 25. Cole J, Spritz RA. The genetics of facial morphology. eLS [Internet]. 2017:[1-9 pp.].
594 26. Cheverud JM, Routman EJ, Irschick DJ. PLEIOTROPIC EFFECTS OF INDIVIDUAL GENE LOCI
595 ON MANDIBULAR MORPHOLOGY. Evolution. 1997;51(6):2006-16. doi: 10.1111/j.1558-
596 5646.1997.tb05122.x. PubMed PMID: 28565113.
597 27. Kenney-Hunt JP, Wang B, Norgard EA, Fawcett G, Falk D, Pletscher LS, et al. Pleiotropic
598 patterns of quantitative trait loci for 70 murine skeletal traits. Genetics. 2008;178(4):2275-88.
599 doi: 10.1534/genetics.107.084434. PubMed PMID: 18430949; PubMed Central PMCID:
600 PMCPMC2323815.
601 28. Pallares LF, Harr B, Turner LM, Tautz D. Use of a natural hybrid zone for genomewide
602 association mapping of craniofacial traits in the house mouse. Mol Ecol. 2014;23(23):5756-70.
603 Epub 2014/11/15. doi: 10.1111/mec.12968. PubMed PMID: 25319559.
604 29. Klingenberg CP, Leamy LJ. Quantitative genetics of geometric shape in the mouse
605 mandible. Evolution. 2001;55(11):2342-52. doi: 10.1111/j.0014-3820.2001.tb00747.x.
606 30. Klingenberg CP, Leamy LJ, Cheverud JM. Integration and Modularity of Quantitative Trait
607 Locus Effects on Geometric Shape in the Mouse Mandible. Genetics. 2004;166(4):1909-21. doi:
608 10.1534/genetics.166.4.1909.
609 31. Flint J, Eskin E. Genome-wide association studies in mice. Nat Rev Genet.
610 2012;13(11):807-17. Epub 2012/10/09. doi: 10.1038/nrg3335. PubMed PMID: 23044826;
611 PubMed Central PMCID: PMCPMC3625632.
612 32. Pallares LF, Carbonetto P, Gopalakrishnan S, Parker CC, Ackert-Bicknell CL, Palmer AA, et
613 al. Mapping of Craniofacial Traits in Outbred Mice Identifies Major Developmental Genes
614 Involved in Shape Determination. PLoS Genet. 2015;11(11):e1005607. Epub 2015/11/02. doi:
615 10.1371/journal.pgen.1005607. PubMed PMID: 26523602; PubMed Central PMCID:
616 PMCPMC4629907.
617 33. Maga AM, Navarro N, Cunningham ML, Cox TC. Quantitative trait loci affecting the 3D
618 skull shape and size in mouse and prioritization of candidate genes in-silico. Front Physiol.
619 2015;6:92. Epub 2015/03/26. doi: 10.3389/fphys.2015.00092. PubMed PMID: 25859222;
620 PubMed Central PMCID: PMCPMC4374467.
621 34. Percival CJ, Green R, Roseman CC, Gatti DM, Morgan JL, Murray SA, et al.
622 Developmental constraint through negative pleiotropy in the zygomatic arch. Evodevo.

623 2018;9:3. Epub 2018/01/27. doi: 10.1186/s13227-018-0092-3. PubMed PMID: 29423138;
624 PubMed Central PMCID: PMCPMC5787316.
625 35. Gudbjartsson DF, Walters GB, Thorleifsson G, Stefansson H, Halldorsson BV,
626 Zusmanovich P, et al. Many sequence variants affecting diversity of adult human height. Nat
627 Genet. 2008;40(5):609-15. Epub 2008/04/06. doi: 10.1038/ng.122. PubMed PMID: 18391951.
628 36. Cole J, Manyama M, Larson JR, Liberton DK, Ferrara TM, Riccardi SL, et al. Human Facial
629 Shape and Size Heritability and Genetic Correlations. Genetics. 2017;205(2):967-78. Epub
630 2016/12/14. doi: 10.1534/genetics.116.193185. PubMed PMID: 27974501; PubMed Central
631 PMCID: PMCPMC5289863.
632 37. de Los Campos G, Vazquez AI, Hsu S, Lello L. Complex-Trait Prediction in the Era of Big
633 Data. Trends Genet. 2018;34(10):746-54. Epub 2018/08/20. doi: 10.1016/j.tig.2018.07.004.
634 PubMed PMID: 30139641; PubMed Central PMCID: PMCPMC6150788.
635 38. Wilderman A, VanOudenhove J, Kron J, Noonan JP, Cotney J. High-Resolution
636 Epigenomic Atlas of Human Embryonic Craniofacial Development. Cell Rep. 2018;23(5):1581-
637 97. doi: 10.1016/j.celrep.2018.03.129. PubMed PMID: 29719267; PubMed Central PMCID:
638 PMCPMC5965702.
639 39. Hooper JE, Feng W, Li H, Leach SM, Phang T, Siska C, et al. Systems biology of facial
640 development: contributions of ectoderm and mesenchyme. Dev Biol. 2017;426(1):97-114. Epub
641 2017/03/29. doi: 10.1016/j.ydbio.2017.03.025. PubMed PMID: 28363736; PubMed Central
642 PMCID: PMCPMC5530582.
643 40. Diez-Roux G, Banfi S, Sultan M, Geffers L, Anand S, Rozado D, et al. A high-resolution
644 anatomical atlas of the transcriptome in the mouse embryo. PLoS Biol. 2011;9(1):e1000582.
645 Epub 2011/01/18. doi: 10.1371/journal.pbio.1000582. PubMed PMID: 21267068; PubMed
646 Central PMCID: PMCPMC3022534.
647 41. Mackay TFC, Stone EA, Ayroles JF. The genetics of quantitative traits: challenges and
648 prospects. Nat Rev Genet. 2009;10(8):565-77. doi:
649 http://www.nature.com/nrg/journal/v10/n8/suppinfo/nrg2612_S1.html.
650 42. Weinberg SM, Roosenboom J, Shaffer JR, Shriver MD, Wysocka J, Claes P. Hunting for
651 genes that shape human faces: Initial successes and challenges for the future. Orthod Craniofac
652 Res. 2019;22 Suppl 1:207-12. doi: 10.1111/ocr.12268. PubMed PMID: 31074157; PubMed
653 Central PMCID: PMCPMC6550302.
654 43. Svenson KL, Gatti DM, Valdar W, Welsh CE, Cheng R, Chesler EJ, et al. High-resolution
655 genetic mapping using the Mouse Diversity outbred population. Genetics. 2012;190(2):437-47.
656 doi: 10.1534/genetics.111.132597. PubMed PMID: 22345611; PubMed Central PMCID:
657 PMCPMC3276626.
658 44. Churchill GA, Gatti DM, Munger SC, Svenson KL. The Diversity Outbred mouse
659 population. Mamm Genome. 2012;23(9-10):713-8. Epub 2012/08/15. doi: 10.1007/s00335-012-
660 9414-2. PubMed PMID: 22892839; PubMed Central PMCID: PMCPMC3524832.
661 45. Chesler EJ, Gatti DM, Morgan AP, Strobel M, Trepanier L, Oberbeck D, et al. Diversity
662 Outbred Mice at 21: Maintaining Allelic Variation in the Face of Selection. G3 (Bethesda).
663 2016;6(12):3893-902. Epub 2016/12/07. doi: 10.1534/g3.116.035527. PubMed PMID:
664 27694113; PubMed Central PMCID: PMCPMC5144960.

46. Yang H, Wang JR, Didion JP, Buus RJ, Bell TA, Welsh CE, et al. Subspecific origin and haplotype diversity in the laboratory mouse. Nat Genet. 2011;43(7):648-55. Epub 2011/05/29. doi: 10.1038/ng.847. PubMed PMID: 21623374; PubMed Central PMCID: PMCPMC3125408.
47. Consortium CC. The genome architecture of the Collaborative Cross mouse genetic reference population. Genetics. 2012;190(2):389-401. doi: 10.1534/genetics.111.132639. PubMed PMID: 22345608; PubMed Central PMCID: PMCPMC3276630.
48. Broman KW, Gatti DM, Simecek P, Furlotte NA, Prins P, Sen Ś, et al. R/qtl2: Software for Mapping Quantitative Trait Loci with High-Dimensional Data and Multiparent Populations. Genetics. 2019;211(2):495-502. Epub 2018/12/27. doi: 10.1534/genetics.118.301595. PubMed PMID: 30591514; PubMed Central PMCID: PMCPMC6366910.
49. Gatti DM, Svenson KL, Shabalin A, Wu LY, Valdar W, Simecek P, et al. Quantitative trait locus mapping methods for diversity outbred mice. G3 (Bethesda). 2014;4(9):1623-33. Epub 2014/09/18. doi: 10.1534/g3.114.013748. PubMed PMID: 25237114; PubMed Central PMCID: PMCPMC4169154.
50. Runcie DE, Mukherjee S. Dissecting High-Dimensional Phenotypes with Bayesian Sparse Factor Analysis of Genetic Covariance Matrices. Genetics. 2013;194(3):753-67. doi: 10.1534/genetics.113.151217.
51. Lander ES, Botstein D. Mapping mendelian factors underlying quantitative traits using RFLP linkage maps. Genetics. 1989;121(1):185-99. PubMed PMID: 2563713; PubMed Central PMCID: PMCPMC1203601.
52. Listgarten J, Lippert C, Kadie CM, Davidson RI, Eskin E, Heckerman D. Improved linear mixed models for genome-wide association studies. Nat Methods. 2012;9(6):525-6. Epub 2012/05/30. doi: 10.1038/nmeth.2037. PubMed PMID: 22669648; PubMed Central PMCID: PMCPMC3597090.
53. Cheng R, Parker CC, Abney M, Palmer AA. Practical considerations regarding the use of genotype and pedigree data to model relatedness in the context of genome-wide association studies. G3 (Bethesda). 2013;3(10):1861-7. Epub 2013/10/03. doi: 10.1534/g3.113.007948. PubMed PMID: 23979941; PubMed Central PMCID: PMCPMC3789811.
54. Yang J, Zaitlen NA, Goddard ME, Visscher PM, Price AL. Advantages and pitfalls in the application of mixed-model association methods. Nat Genet. 2014;46(2):100-6. doi: 10.1038/ng.2876. PubMed PMID: 24473328; PubMed Central PMCID: PMCPMC3989144.
55. Tsagkrasoulis D, Hysi P, Spector T, Montana G. Heritability maps of human face morphology through large-scale automated three-dimensional phenotyping. Sci Rep. 2017;7:45885. Epub 2017/04/19. doi: 10.1038/srep45885. PubMed PMID: 28422179; PubMed Central PMCID: PMCPMC5395823.
56. Marroig G, Melo DA, Garcia G. Modularity, noise, and natural selection. Evolution. 2012;66(5):1506-24.
57. Mrode RA. Linear models for the prediction of animal breeding values. 3rd ed. Oxfordshire, UK: CABI; 2014.
58. Robinson GK. That BLUP is a good thing: the estimation of random effects. Statistical Science. 1991;6(1):15-51. doi: 10.1214/ss/1177011933.
59. Hallgrimsson B, Katz DC, Aponte JD, Larson JE, Devine J, Gonzalez P, et al. Integration and the developmental genetics of allometry. Integrative and Comparative Biology. 2019, in press.

60. Jolicoeur P, Mosimann JE. Size and shape variation in the painted turtle. A principal component analysis. Growth. 1960;24:339-54. PubMed PMID: 13790416.
61. Mitteroecker P, Gunz P, Bernhard M, Schaefer K, Bookstein F. Comparison of cranial ontogenetic trajectories among great apes and humans. Journal of Human Evolution. 2004;46(6):679-98. doi: 10.1016/j.jhevol.2004.03.006.
62. Mosimann JE. Size allometry: Size and shape variables with characterizations of the lognormal and generalized gamma distributions. Journal of the American Statistical Association. 1970;65:930-45.
63. Cheverud JM. Relationships among ontogenetic, static, and evolutionary allometry. Am J Phys Anthropol. 1982;59(2):139-49. doi: 10.1002/ajpa.1330590204. PubMed PMID: 7149015.
64. Larson JR, Manyama MF, Cole JB, Gonzalez PN, Percival CJ, Liberton DK, et al. Body size and allometric variation in facial shape in children. Am J Phys Anthropol. 2018;165(2):327-42. Epub 2017/11/27. doi: 10.1002/ajpa.23356. PubMed PMID: 29178597; PubMed Central PMCID: PMCPMC5777898.
65. Goios A, Pereira L, Bogue M, Macaulay V, Amorim A. mtDNA phylogeny and evolution of laboratory mouse strains. Genome Res. 2007;17(3):293-8. Epub 2007/02/06. doi: 10.1101/gr.5941007. PubMed PMID: 17284675; PubMed Central PMCID: PMCPMC1800920.
66. Logan RW, Robledo RF, Recla JM, Philip VM, Bubier JA, Jay JJ, et al. High-precision genetic mapping of behavioral traits in the diversity outbred mouse population. Genes Brain Behav. 2013;12(4):424-37. Epub 2013/03/20. doi: 10.1111/gbb.12029. PubMed PMID: 23433259; PubMed Central PMCID: PMCPMC3709837.
67. French JE, Gatti DM, Morgan DL, Kissling GE, Shockley KR, Knudsen GA, et al. Diversity Outbred Mice Identify Population-Based Exposure Thresholds and Genetic Factors that Influence Benzene-Induced Genotoxicity. Environ Health Perspect. 2015;123(3):237-45. Epub 2014/11/06. doi: 10.1289/ehp.1408202. PubMed PMID: 25376053; PubMed Central PMCID: PMCPMC4348743.
68. Smallwood TL, Gatti DM, Quizon P, Weinstock GM, Jung KC, Zhao L, et al. High-resolution genetic mapping in the diversity outbred mouse population identifies Apobec1 as a candidate gene for atherosclerosis. G3 (Bethesda). 2014;4(12):2353-63. Epub 2014/10/23. doi: 10.1534/g3.114.014704. PubMed PMID: 25344410; PubMed Central PMCID: PMCPMC4267931.
69. Shorter JR, Huang W, Beak JY, Hua K, Gatti DM, de Villena FP, et al. Quantitative trait mapping in Diversity Outbred mice identifies two genomic regions associated with heart size. Mamm Genome. 2018;29(1-2):80-9. Epub 2017/12/26. doi: 10.1007/s00335-017-9730-7. PubMed PMID: 29279960; PubMed Central PMCID: PMCPMC6340297.
70. Bressler J, Tsai TF, Wu MY, Tsai SF, Ramirez MA, Armstrong D, et al. The SNRPN promoter is not required for genomic imprinting of the Prader-Willi/Angelman domain in mice. Nat Genet. 2001;28(3):232-40. doi: 10.1038/90067. PubMed PMID: 11431693.
71. Albrecht U, Sutcliffe JS, Cattanach BM, Beechey CV, Armstrong D, Eichele G, et al. Imprinted expression of the murine Angelman syndrome gene, Ube3a, in hippocampal and Purkinje neurons. Nat Genet. 1997;17(1):75-8. doi: 10.1038/ng0997-75. PubMed PMID: 9288101.
72. Kobayashi S, Kohda T, Ichikawa H, Ogura A, Ohki M, Kaneko-Ishino T, et al. Paternal expression of a novel imprinted gene, Peg12/Frat3, in the mouse 7C region homologous to the

752 Prader-Willi syndrome region. Biochem Biophys Res Commun. 2002;290(1):403-8. doi:
753 10.1006/bbrc.2001.6160. PubMed PMID: 11779183.
754 73. Morison IM, Ramsay JP, Spencer HG. A census of mammalian imprinting. Trends Genet.
755 2005;21(8):457-65. doi: 10.1016/j.tig.2005.06.008. PubMed PMID: 15990197.
756 74. Gray TA, Saitoh S, Nicholls RD. An imprinted, mammalian bicistronic transcript encodes
757 two independent proteins. Proc Natl Acad Sci U S A. 1999;96(10):5616-21. doi:
758 10.1073/pnas.96.10.5616. PubMed PMID: 10318933; PubMed Central PMCID: PMCPMC21909.
759 75. Knoll JH, Nicholls RD, Magenis RE, Graham JM, Lalande M, Latt SA. Angelman and
760 Prader-Willi syndromes share a common chromosome 15 deletion but differ in parental origin
761 of the deletion. Am J Med Genet. 1989;32(2):285-90. doi: 10.1002/ajmg.1320320235. PubMed
762 PMID: 2564739.
763 76. Mic FA, Molotkov A, Fan X, Cuenca AE, Duester G. RALDH3, a retinaldehyde
764 dehydrogenase that generates retinoic acid, is expressed in the ventral retina, otic vesicle and
765 olfactory pit during mouse development. Mech Dev. 2000;97(1-2):227-30. doi: 10.1016/s0925-
766 4773(00)00434-2. PubMed PMID: 11025231.
767 77. Visel A, Thaller C, Eichele G. GenePaint.org: an atlas of gene expression patterns in the
768 mouse embryo. Nucleic Acids Res. 2004;32(Database issue):D552-6. doi: 10.1093/nar/gkh029.
769 PubMed PMID: 14681479; PubMed Central PMCID: PMCPMC308763.
770 78. Martin KM, Metcalfe JC, Kemp PR. Expression of Klf9 and Klf13 in mouse development.
771 Mech Dev. 2001;103(1-2):149-51. doi: 10.1016/s0925-4773(01)00343-4. PubMed PMID:
772 11335124.
773 79. Yokoyama S, Ito Y, Ueno-Kudoh H, Shimizu H, Uchibe K, Albini S, et al. A systems
774 approach reveals that the myogenesis genome network is regulated by the transcriptional
775 repressor RP58. Dev Cell. 2009;17(6):836-48. doi: 10.1016/j.devcel.2009.10.011. PubMed PMID:
776 20059953; PubMed Central PMCID: PMCPMC3110151.
777 80. Unda FJ, Pérez-Nanclares G, Le Morvan V, Hernández C, Vilaxa A, De-la-Fuente M, et al.
778 Dynamic assembly of tight junction-associated proteins ZO-1, ZO-2, ZO-3 and occludin during
779 mouse tooth development. Histol Histopathol. 2003;18(1):27-38. doi: 10.14670/HH-18.27.
780 PubMed PMID: 12507281.
781 81. Yoshida T, Miyoshi J, Takai Y, Thesleff I. Cooperation of nectin-1 and nectin-3 is required
782 for normal ameloblast function and crown shape development in mouse teeth. Dev Dyn.
783 2010;239(10):2558-69. doi: 10.1002/dvdy.22395. PubMed PMID: 21038445.
784 82. de Koning DJ, Bovenhuis H, van Arendonk JA. On the detection of imprinted quantitative
785 trait loci in experimental crosses of outbred species. Genetics. 2002;161(2):931-8. PubMed
786 PMID: 12072486; PubMed Central PMCID: PMCPMC1462155.
787 83. Cheverud JM, Hager R, Roseman C, Fawcett G, Wang B, Wolf JB. Genomic imprinting
788 effects on adult body composition in mice. Proc Natl Acad Sci U S A. 2008;105(11):4253-8. Epub
789 2008/03/12. doi: 10.1073/pnas.0706562105. PubMed PMID: 18337500; PubMed Central
790 PMCID: PMCPMC2393747.
791 84. Leamy LJ, Klingenberg CP, Sherratt E, Wolf JB, Cheverud JM. A search for quantitative
792 trait loci exhibiting imprinting effects on mouse mandible size and shape. Heredity (Edinb).
793 2008;101(6):518-26. Epub 2008/08/06. doi: 10.1038/hdy.2008.79. PubMed PMID: 18685568.

794 85. Holm VA, Cassidy SB, Butler MG, Hanchett JM, Greenswag LR, Whitman BY, et al.
795 Prader-Willi syndrome: consensus diagnostic criteria. Pediatrics. 1993;91(2):398-402. PubMed
796 PMID: 8424017; PubMed Central PMCID: PMCPMC6714046.
797 86. Katz DC, Grote MN, Weaver TD. Changes in human skull morphology across the
798 agricultural transition are consistent with softer diets in preindustrial farming groups. Proc Natl
799 Acad Sci U S A. 2017;114(34):9050-5. Epub 2017/07/24. doi: 10.1073/pnas.1702586114.
800 PubMed PMID: 28739900; PubMed Central PMCID: PMCPMC5576786.
801 87. Liberzon A, Subramanian A, Pinchback R, Thorvaldsdóttir H, Tamayo P, Mesirov JP.
802 Molecular signatures database (MSigDB) 3.0. Bioinformatics. 2011;27(12):1739-40. Epub
803 2011/05/05. doi: 10.1093/bioinformatics/btr260. PubMed PMID: 21546393; PubMed Central
804 PMCID: PMCPMC3106198.
805 88. Le N, Nagarajan R, Wang JY, Svaren J, LaPash C, Araki T, et al. Nab proteins are essential
806 for peripheral nervous system myelination. Nat Neurosci. 2005;8(7):932-40. PubMed PMID:
807 16136673.
808 89. Shi C, Sakuma M, Mooroka T, Liscoe A, Gao H, Croce KJ, et al. Down-regulation of the
809 forkhead transcription factor Foxp1 is required for monocyte differentiation and macrophage
810 function. Blood. 2008;112(12):4699-711. Epub 2008/09/17. doi: 10.1182/blood-2008-01-
811 137018. PubMed PMID: 18799727; PubMed Central PMCID: PMCPMC2597137.
812 90. Zhao H, Zhou W, Yao Z, Wan Y, Cao J, Zhang L, et al. Foxp1/2/4 regulate endochondral
813 ossification as a suppresser complex. Dev Biol. 2015;398(2):242-54. Epub 2014/12/17. doi:
814 10.1016/j.ydbio.2014.12.007. PubMed PMID: 25527076; PubMed Central PMCID:
815 PMCPMC4342236.
816 91. Pacheco-Costa R, Kadakia JR, Atkinson EG, Wallace JM, Plotkin LI, Reginato RD.
817 Connexin37 deficiency alters organic bone matrix, cortical bone geometry, and increases
818 Wnt/β-catenin signaling. Bone. 2017;97:105-13. Epub 2017/01/16. doi:
819 10.1016/j.bone.2017.01.010. PubMed PMID: 28096061.
820 92. Wilson DG, Phamluong K, Lin WY, Barck K, Carano RA, Diehl L, et al. Chondroitin sulfate
821 synthase 1 (Chsy1) is required for bone development and digit patterning. Dev Biol.
822 2012;363(2):413-25. Epub 2012/01/17. doi: 10.1016/j.ydbio.2012.01.005. PubMed PMID:
823 22280990.
824 93. Xing WR, Goodluck H, Zeng C, Mohan S. Role and mechanism of action of leucine-rich
825 repeat kinase 1 in bone. Bone Res. 2017;5:17003. Epub 2017/03/14. doi:
826 10.1038/boneres.2017.3. PubMed PMID: 28326224; PubMed Central PMCID:
827 PMCPMC5348726.
828 94. Vecchione L, Byron C, Cooper GM, Barbano T, Hamrick MW, Sciote JJ, et al. Craniofacial
829 morphology in myostatin-deficient mice. J Dent Res. 2007;86(11):1068-72. doi:
830 10.1177/154405910708601109. PubMed PMID: 17959898.
831 95. Vecchione L, Miller J, Byron C, Cooper GM, Barbano T, Cray J, et al. Age-related changes
832 in craniofacial morphology in GDF-8 (myostatin)-deficient mice. Anat Rec (Hoboken).
833 2010;293(1):32-41. doi: 10.1002/ar.21024. PubMed PMID: 19899116; PubMed Central PMCID:
834 PMCPMC3113544.
835 96. Sahni M, Ambrosetti DC, Mansukhani A, Gertner R, Levy D, Basilico C. FGF signaling
836 inhibits chondrocyte proliferation and regulates bone development through the STAT-1
837 pathway. Genes & Development. 1999;13:1361-6.

838 97. Xiao L, Naganawa T, Obugunde E, Gronowicz G, Ornitz DM, Coffin JD, et al. Stat1
839 controls postnatal bone formation by regulating fibroblast growth factor signaling in
840 osteoblasts. J Biol Chem. 2004;279(26):27743-52. Epub 2004/04/08. doi:
841 10.1074/jbc.M314323200. PubMed PMID: 15073186.
842 98. Kim S, Koga T, Isobe M, Kern BE, Yokochi T, Chin YE, et al. Stat1 functions as a
843 cytoplasmic attenuator of Runx2 in the transcriptional program of osteoblast differentiation.
844 Genes Dev. 2003;17(16):1979-91. doi: 10.1101/gad.1119303. PubMed PMID: 12923053;
845 PubMed Central PMCID: PMCPMC196253.
846 99. Le Fevre AK, Taylor S, Malek NH, Horn D, Carr CW, Abdul-Rahman OA, et al. FOXP1
847 mutations cause intellectual disability and a recognizable phenotype. Am J Med Genet A.
848 2013;161A(12):3166-75. Epub 2013/09/24. doi: 10.1002/ajmg.a.36174. PubMed PMID:
849 24214399.
850 100. Tian J, Ling L, Shboul M, Lee H, O'Connor B, Merriman B, et al. Loss of CHSY1, a secreted
851 FRINGE enzyme, causes syndromic brachydactyly in humans via increased NOTCH signaling. Am
852 J Hum Genet. 2010;87(6):768-78. doi: 10.1016/j.ajhg.2010.11.005. PubMed PMID: 21129727;
853 PubMed Central PMCID: PMCPMC2997365.
854 101. Huh A, Horton MJ, Cuenco KT, Raoul G, Rowlerson AM, Ferri J, et al. Epigenetic influence
855 of KAT6B and HDAC4 in the development of skeletal malocclusion. Am J Orthod Dentofacial
856 Orthop. 2013;144(4):568-76. doi: 10.1016/j.ajodo.2013.06.016. PubMed PMID: 24075665;
857 PubMed Central PMCID: PMCPMC3849704.
858 102. Vimalraj S, Arumugam B, Miranda PJ, Selvamurugan N. Runx2: Structure, function, and
859 phosphorylation in osteoblast differentiation. Int J Biol Macromol. 2015;78:202-8. Epub
860 2015/04/13. doi: 10.1016/j.ijbiomac.2015.04.008. PubMed PMID: 25881954.
861 103. Clayton-Smith J, O'Sullivan J, Daly S, Bhaskar S, Day R, Anderson B, et al. Whole-exome-
862 sequencing identifies mutations in histone acetyltransferase gene KAT6B in individuals with the
863 Say-Barber-Biesecker variant of Ohdo syndrome. Am J Hum Genet. 2011;89(5):675-81. doi:
864 10.1016/j.ajhg.2011.10.008. PubMed PMID: 22077973; PubMed Central PMCID:
865 PMCPMC3213399.
866 104. Sena K, Morotome Y, Baba O, Terashima T, Takano Y, Ishikawa I. Gene expression of
867 growth differentiation factors in the developing periodontium of rat molars. J Dent Res.
868 2003;82(3):166-71. doi: 10.1177/154405910308200304. PubMed PMID: 12598543.
869 105. Nakashima M, Toyono T, Murakami T, Akamine A. Transforming growth factor-beta
870 superfamily members expressed in rat incisor pulp. Arch Oral Biol. 1998;43(9):745-51. doi:
871 10.1016/s0003-9969(98)00046-6. PubMed PMID: 9783830.
872 106. Cerny R, Cattell M, Sauka-Spengler T, Bronner-Fraser M, Yu F, Medeiros DM. Evidence
873 for the prepattern/cooption model of vertebrate jaw evolution. Proc Natl Acad Sci U S A.
874 2010;107(40):17262-7. Epub 2010/09/20. doi: 10.1073/pnas.1009304107. PubMed PMID:
875 20855630; PubMed Central PMCID: PMCPMC2951391.
876 107. So PL, Danielian PS. Cloning and expression analysis of a mouse gene related to
877 Drosophila odd-skipped. Mech Dev. 1999;84(1-2):157-60. PubMed PMID: 10473132.
878 108. Kawai S, Yamauchi M, Amano A. Zinc-finger transcription factor Odd-skipped related 1
879 regulates cranial bone formation. J Bone Miner Metab. 2018;36(6):640-7. Epub 2017/12/12.
880 doi: 10.1007/s00774-017-0885-9. PubMed PMID: 29234951.

881 109. Jeong J, Cesario J, Zhao Y, Burns L, Westphal H, Rubenstein JL. Cleft palate defect of
882 Dlx1/2-/- mutant mice is caused by lack of vertical outgrowth in the posterior palate. Dev Dyn.
883 2012;241(11):1757-69. Epub 2012/09/28. doi: 10.1002/dvdy.23867. PubMed PMID: 22972697;
884 PubMed Central PMCID: PMCPMC3988582.
885 110. Zelzer E, McLean W, Ng YS, Fukai N, Reginato AM, Lovejoy S, et al. Skeletal defects in
886 VEGF(120/120) mice reveal multiple roles for VEGF in skeletogenesis. Development.
887 2002;129(8):1893-904. PubMed PMID: 11934855.
888 111. R Development Core Team. R: A language and environment for statistical computing. R
889 Foundation for Statistical Computing, Vienna, Austria. URL http://www.R-project.org/2015.
890 112. Mitteroecker P, Gunz P. Advances in Geometric Morphometrics. Evolutionary Biology.
891 2009;36(2):235-47. doi: 10.1007/s11692-009-9055-x.
892 113. Schlager S. Morpho and Rvcg – Shape Analysis in R. In: Zheng G, Li S, Szekely G, editors.
893 Statistical Shape and Deformation Analysis: Academic Press; 2017. p. 217-56.
894 114. Mardia KV, Bookstein FL, Moreton IJ. Statistical assessment of bilateral symmetry of
895 shapes. Biometrika. 2000;87(2):285-300.
896 115. Klingenberg CP, Barluenga M, Meyer A. Shape analysis of symmetric structures:
897 quantifying variation among individuals and asymmetry. Evolution. 2002;56(10):1909-20.
898 PubMed PMID: 12449478.
899 116. Morgan AP, Fu CP, Kao CY, Welsh CE, Didion JP, Yadgary L, et al. The Mouse Universal
900 Genotyping Array: From Substrains to Subspecies. G3 (Bethesda). 2015;6(2):263-79. Epub
901 2015/12/18. doi: 10.1534/g3.115.022087. PubMed PMID: 26684931; PubMed Central PMCID:
902 PMCPMC4751547.
903 117. Didion JP, Morgan AP, Clayshulte AM, Mcmullan RC, Yadgary L, Petkov PM, et al. A
904 multi-megabase copy number gain causes maternal transmission ratio distortion on mouse
905 chromosome 2. PLoS Genet. 2015;11(2):e1004850. Epub 2015/02/13. doi:
906 10.1371/journal.pgen.1004850. PubMed PMID: 25679959; PubMed Central PMCID:
907 PMCPMC4334553.
908 118. Cardon LR, Palmer LJ. Population stratification and spurious allelic association. Lancet.
909 2003;361(9357):598-604. doi: 10.1016/S0140-6736(03)12520-2. PubMed PMID: 12598158.
910 119. Broman KW, Gatti DM, Svenson KL, Sen Ś, Churchill GA. Cleaning Genotype Data from
911 Diversity Outbred Mice. G3 (Bethesda). 2019;9(5):1571-9. Epub 2019/05/07. doi:
912 10.1534/g3.119.400165. PubMed PMID: 30877082; PubMed Central PMCID: PMCPMC6505173.
913 120. Sybert VP, McCauley E. Turner's syndrome. N Engl J Med. 2004;351(12):1227-38. doi:
914 10.1056/NEJMra030360. PubMed PMID: 15371580.
915 121. Hallgrimsson BA, J David, Katz DC, Bannister JJ, Riccardi SL, Mahasuwan N, McInnes BL,
916 et al. Automated syndrome diagnosis by three-dimensional facial photogrammetric imaging.
917 American Journal of Human Genetics. 2019, in review.
918 122. Krzanowski WJ. Principles of Multivariate Analysis: A User's Perspective. New York:
919 Oxford University Press; 2005.
920 123. Churchill GA, Doerge RW. Empirical threshold values for quantitative trait mapping.
921 Genetics. 1994;138(3):963-71. PubMed PMID: 7851788; PubMed Central PMCID:
922 PMCPMC1206241.
923 124. Manichaikul A, Dupuis J, Sen S, Broman KW. Poor performance of bootstrap confidence
924 intervals for the location of a quantitative trait locus. Genetics. 2006;174(1):481-9. Epub

925 2006/06/18. doi: 10.1534/genetics.106.061549. PubMed PMID: 16783000; PubMed Central
926 PMCID: PMCPMC1569776.
927 125. Yalcin B, Flint J, Mott R. Using progenitor strain information to identify quantitative trait
928 nucleotides in outbred mice. Genetics. 2005;171(2):673-81. Epub 2005/08/05. doi:
929 10.1534/genetics.104.028902. PubMed PMID: 16085706; PubMed Central PMCID:
930 PMCPMC1456780.
931 126. Baud A, Hermsen R, Guryev V, Stridh P, Graham D, McBride MW, et al. Combined
932 sequence-based and genetic mapping analysis of complex traits in outbred rats. Nat Genet.
933 2013;45(7):767-75. Epub 2013/05/26. doi: 10.1038/ng.2644. PubMed PMID: 23708188;
934 PubMed Central PMCID: PMCPMC3821058.
935 127. Rhee SY, Wood V, Dolinski K, Draghici S. Use and misuse of the gene ontology
936 annotations. Nat Rev Genet. 2008;9(7):509-15. Epub 2008/05/13. doi: 10.1038/nrg2363.
937 PubMed PMID: 18475267.
938 128. Maglott D, Ostell J, Pruitt KD, Tatusova T. Entrez Gene: gene-centered information at
939 NCBI. Nucleic Acids Res. 2011;39(Database issue):D52-7. Epub 2010/11/28. doi:
940 10.1093/nar/gkq1237. PubMed PMID: 21115458; PubMed Central PMCID: PMCPMC3013746.
941 129. Subramanian A, Tamayo P, Mootha VK, Mukherjee S, Ebert BL, Gillette MA, et al. Gene
942 set enrichment analysis: a knowledge-based approach for interpreting genome-wide expression
943 profiles. Proc Natl Acad Sci U S A. 2005;102(43):15545-50. Epub 2005/09/30. doi:
944 10.1073/pnas.0506580102. PubMed PMID: 16199517; PubMed Central PMCID:
945 PMCPMC1239896.
946 130. Katz DC, Grote MN, Weaver TD. A mixed model for the relationship between climate
947 and cranial form. American Journal of Physical Anthropology. 2016;160:593-603.
948 131. Mitteroecker P, Cheverud JM, Pavlicev M. Multivariate Analysis of Genotype-Phenotype
949 Association. Genetics. 2016. doi: 10.1534/genetics.115.181339.
950 132. Nakagawa S, Schielzeth H. A general and simple method for obtaining $R^2$ from
951 generalized linear mixed-effects models. Methods in Ecology and Evolution. 2013;4:133-42. doi:
952 10.1111/j.2041-210x.2012.00261.x.
953 133. Adler D, Murdoch D, others. rgl: 3D Visualization Using OpenGL. 0.95.1441 ed2016.
954 134. Rohlf FJ. Shape statistics: Procrustes superimpositions and tangent spaces. Journal of
955 Classification. 1999;16(2):197-223.
956

957 ## Supporting Information

958 **S1 Fig. Eigenvalue decay**. Percentage of total variation explained for each shape principal

959 component. We performed genome scans for all PCs explaining more than 1% of shape

960 variation (red point identifies cutoff at PC 20) and subjected the first five PCs (green point

961 identifies PC 5 floor) to in-depth analysis.

962 **S2 Fig. Change in chromosome 2 WSB allele frequencies over generations.** Sample-wide WSB
963 allele frequency on chromosome 2 by DO generation. The high WSB allele frequency in earlier
964 generations reflects meiotic drive for WSB at the *R2d2* locus. Declining frequencies in later
965 generations reflect the systematic purge of WSB alleles from the DO population.
966 **S1 Table.** LOD peaks and support intervals for all QTL on PCs 1-20.
967 **S2 Table.** Full array of LOCO mean heritabilities over PCs 1-20.
968 **S1 File. Genes, PCs 1-5.** All named, protein-coding genes in the PC 1-5 QTL intervals.
969 **S2 File. Top GO annotations, PCs 1-5.** Top 100 FDR q-value GO terms for the PC 1-5 QTL interval
970 gene set (Molecular Signatures Database output file).
971 **S3 File. Top GO annotations, PC 1.** For the PC1 QTL interval gene set, GO terms with FDR q-
972 value < 0.05 (Molecular Signatures Database output file).
973